


FA-PEG Modified ZIF(Mn) Nanoparticles Loaded with Baicalin for Imaging-Guided Treatment of Melanoma in Mice

Dong Zhang , Mogen Zhang, Huiping Fan, Rui Sun, Jiayun Liu, Weiyuan Ma

Department of Dermatology, Affiliated Hospital of Shandong Second Medical University, School of Clinical Medicine, Shandong Second Medical University, Weifang, 261031, People's Republic of China

Correspondence: Weiyuan Ma, Email fymaweiyuan@sdsu.edu.cn

Background: Melanoma is an aggressive skin tumor with limited therapeutic options due to rapid proliferation, early metastasis, and poor prognosis. Baicalin (BA), a natural flavonoid, shows promise in inducing ferroptosis and apoptosis but faces challenges of poor solubility and bioavailability. To address these issues, we developed a multifunctional drug delivery system: manganese-doped ZIF-8 nanoparticles (ZIF(Mn)) loaded with BA and modified with folic acid (FA) and polyethylene glycol (PEG). FA targets melanoma cells by exploiting folate receptor overexpression, while PEG enhances biocompatibility and systemic circulation. Manganese enables magnetic resonance (MR) imaging for real-time, non-invasive therapy monitoring.

Methods: BA-loaded ZIF(Mn)/FA-PEG nanoparticles were synthesized via a one-pot method, enabling drug encapsulation, Mn^{2+} incorporation, and surface modification. The nanoparticles were comprehensively characterized (particle size, Zeta potential, FTIR, and XRD). Cytotoxicity and cellular uptake were evaluated in B16-F10 melanoma cells, and in vivo experiments in C57BL/6J mice investigated MR imaging capability, antitumor efficacy, and biosafety.

Results: BA@ZIF(Mn)/FA-PEG nanoparticles demonstrated excellent stability, a BA loading capacity of $33.50 \pm 0.04\%$, and pH-responsive release, with accelerated drug release under acidic tumor conditions. Mn^{2+} provided strong T1-weighted MR imaging contrast. Cellular and animal studies showed enhanced uptake, reduced premature drug release, and improved compatibility. Mechanistically, the nanoparticles induced significant ferroptosis and apoptosis in melanoma cells, leading to potent antitumor effects.

Conclusion: The BA@ZIF(Mn)/FA-PEG nanoplateform effectively integrates targeted delivery, imaging guidance, and dual ferroptosis-apoptosis induction, offering a promising strategy for improving melanoma treatment outcomes.

Keywords: Baicalin, melanoma, metal-organic frameworks, folic acid targeted, magnetic resonance imaging, ferroptosis

Introduction

Cutaneous malignant melanoma (CMM) originates from neuroectodermal melanocytes in the basal layer of the epidermis and represents a significant health burden due to its high malignancy, rapid progression, and propensity for early metastasis.¹ Despite advances in diagnostic techniques and treatment modalities, CMM remains challenging to manage, particularly in advanced stages where therapeutic options are limited and prognosis is poor.² The incidence of CMM continues to rise globally, reflecting both environmental factors such as ultraviolet radiation exposure and genetic predispositions. In the United States alone, the incidence rate of CMM has steadily increased, with an annual growth rate underscoring the need for novel therapeutic strategies.³ Current clinical management relies heavily on surgical resection combined with adjuvant therapies, including chemotherapy, targeted therapy directed against BRAF mutations, and immunotherapy utilizing checkpoint inhibitors. While these approaches have improved outcomes, challenges persist, particularly in patients with advanced disease stages characterized by resistance to conventional treatments.⁴⁻⁶

BA, a bioactive flavonoid isolated from traditional Chinese medicine, has garnered attention for its anticancer properties, including the induction of ferroptosis and apoptosis in various cancer models.⁷⁻¹⁰ However, its clinical utility

is hindered by poor aqueous solubility, slow dissolution kinetics, and limited bioavailability. Overcoming these challenges is crucial to enhancing its therapeutic efficacy against melanoma.^{11,12} Recent studies have demonstrated that BA exhibits significant antitumor effects in melanoma by inhibiting cell proliferation and promoting apoptosis, highlighting its potential as a therapeutic agent.¹³

Recent advancements in nanotechnology have paved the way for innovative drug delivery systems capable of improving the pharmacokinetics and targeting capabilities of therapeutic agents.¹⁴ Among these systems, FA-PEG modified NPs have emerged as effective platforms for targeted drug delivery.^{15,16} The incorporation of FA enhances the specificity of drug delivery to folate receptor-expressing cells, such as melanoma cells, facilitating improved therapeutic outcomes.^{14,17} Additionally, manganese (Mn^{2+}) has been shown to enhance the imaging capabilities of NPs, enabling precise localization within tumor tissues using magnetic resonance (MR) imaging.^{18,19} This combination of FA-PEG and Mn^{2+} not only improves targeting efficiency but also allows for real-time monitoring of drug distribution and therapeutic efficacy.

Metal-organic frameworks (MOFs), characterized by their high porosity, tunable structures, and biocompatibility, have emerged as promising candidates for drug delivery applications. Zinc-based MOFs, such as zeolitic imidazolate framework NPs (ZIF-8), exhibit exceptional stability under physiological conditions and pH-responsive drug release profiles, making them suitable for targeted delivery in cancer therapy.²⁰ This study focuses on the development of manganese-doped ZIF-8 NPs (ZIF(Mn)) functionalized with FA-PEG as a novel drug delivery platform for BA. The incorporation of manganese enhances the imaging capabilities of these NPs, facilitating precise localization within tumor tissues. The synergistic combination of targeted drug delivery and imaging guidance represents a cutting-edge approach to improving therapeutic outcomes in melanoma treatment.

Materials and Methods

Reagents

Zinc nitrate hexahydrate ($Zn(NO_3)_2 \cdot 6H_2O$, CAS No. 10196–18-6) was purchased from Damao Chemical Reagent Factory (Tianjin, China), while 2-methylimidazole (2-MeIm, CAS No. 693–98-1) was obtained from Aladdin Biochemical Technology Co., Ltd. (Shanghai, China). Manganese(II) nitrate hexahydrate ($Mn(NO_3)_2 \cdot 6H_2O$, CAS No. 17141–63-8), Baicalin (CAS No. 21967–41-9), N-hydroxysuccinimide (NHS, CAS No. 6066–82-6), 3-dimethylamino-propyl-1-ethylcarbodiimide hydrochloride (EDCI, CAS No. 25952–53-8), 4-dimethylaminopyridine (DMAP, CAS No. 1122–58-3), CH₃O-PEG2K-OH (CAS No. 80506–64-5), and triethylamine (TEA, CAS No. 122–44-8) were obtained from Macklin Biochemical Technology Co., Ltd. (Shanghai, China). Dimethyl sulfoxide (DMSO, CAS No. 67–68-5) and methanol (CAS No. 67–56-1) were sourced from Sinopharm Chemical Reagent Co., Ltd. (Shanghai, China). Dialysis membranes MD44 (3500D, Cat No. YA1078) were purchased from Solarbio Science & Technology Co., Ltd. (Beijing, China).

Horseradish peroxidase (HRP)-labeled goat anti-rabbit IgG, electrochemiluminescence (ECL) reagents, and BCA Protein Assay Kit were obtained from Beyotime Biotechnology (Shanghai, China). The FOLR2 polyclonal antibody (Cat No. 31264-1-AP) was sourced from Proteintech (Wuhan, China). Rabbit anti-mouse glutathione peroxidase 4 (GPX4) (Cat No. 381958), anti-mouse ferritin heavy chain (FTH1) (Cat No. R23306), anti-mouse prostaglandin-endoperoxide synthase 2 (Cat No. R23971), anti-mouse long-chain fatty acid CoA ligase 4 (ACSL4) (Cat No. R24265), and anti-mouse alpha-tubulin (Cat No. 250009) antibodies were purchased from Zenbio (Chengdu, China). RIPA lysis solution, tris-buffered saline with Tween-20, skim milk powder, sodium dodecyl sulfate-polyacrylamide gel electrophoresis (SDS-PAGE) precast gels, and ECL chemiluminescent reagents were acquired from Sparkjade Biotechnology Co., Ltd. (Jinan, China).

Dulbecco's modified Eagle's medium (DMEM) was obtained from Sangon Biotech (Shanghai, China). Fetal bovine serum (FBS) was purchased from Gibco Life Sciences Co., Ltd. (New York, USA). Trypsin/EDTA solution (Cat No. TE2004Y), phosphate-buffered saline (PBS, Cat No. PB2004Y), and RPMI 1640 medium (Cat No. HY1640) were supplied by Haoyang Huake Biotechnology Co., Ltd. (Tianjin, China). FITC Annexin V Apoptosis Detection Kit I (Mat No. 556547) was sourced from BD Biosciences (New York, USA). The cell malondialdehyde (MDA) assay kit

(colorimetric method, Cat No. A003-4-1) was obtained from Nanjing Jiancheng Bioengineering Institute (Nanjing, China).

The Trizol Plus RNA Purification Kit (Cat No. 12183555) was purchased from Thermo Fisher Scientific Inc. (Massachusetts, USA). MightyScript Plus First Strand cDNA Synthesis Master Mix (gDNA digester, Cat No. B639252) and SGExcel FastSYBR Mixture (Cat No. B532955) were provided by Sangon Biotech (Shanghai, China). The Calcein/PI Cell Viability/Cytotoxicity Assay Kit (Cat No. C2015), reactive oxygen species assay kit (Cat No. S0033), colorimetric TUNEL apoptosis assay kit (Cat No. C1091), antifade mounting medium (Cat No. P0126), proteinase K (Cat No. ST533), and hematoxylin staining solution (Cat No. C0107) were purchased from Beyotime Biotechnology (Shanghai, China). Enhanced Cell Counting Kit-8 (Enhanced CCK-8, Cat No. CT0001), EDTA buffer (pH 8.0, Cat No. EE0004), goat serum blocking solution (Cat No. EE0008), and diaminobenzidine chromogenic kit (DAB, Cat No. EE0017) were obtained from Sparkjade Biotechnology Co., Ltd. (Jinan, China).

Animals

Female C57BL/6J Nifdc mice (6–8 weeks old) were housed in a temperature-controlled room with proper light-dark cycles, fed a standard diet, and maintained by the Experimental Animal Center, Shandong Second Medical University (Weifang, China). All animal experiments were conducted following the Guide for the Care and Use of Laboratory Animals published by Shandong Second Medical University (Weifang, China) and approved by its Animal Experimental Ethics Committee. The principles of 3R (reduction, replacement, refinement) were strictly followed to minimize animal suffering.

Cell Culture

The B16-F10 cell line was selected for its well-documented use in melanoma research as a robust preclinical model. Its aggressive tumorigenicity and metastatic potential, coupled with its compatibility with syngeneic mouse models, make it ideal for studying the therapeutic efficacy of novel treatments. Furthermore, its extensive use in previous studies ensures the comparability and reproducibility of the findings.^{14,21,22} As a non-cancerous cell line, L929 is widely used in cytotoxicity assessments due to its established sensitivity to toxic agents and its relevance as a representative model of normal fibroblast cells.²³ B16-F10 mouse melanoma cells and L929 mouse fibroblasts were obtained from Procell Biotechnology Co., Ltd. (Wuhan, China). B16-F10 cells were cultured in RPMI 1640 medium supplemented with 10% FBS, while L929 cells were cultured in DMEM medium supplemented with 10% FBS. The cells were maintained at 37 °C and 5% CO₂ in a humidified incubator with medium changes every 1–2 days.

Synthesis of Manganese-Doped ZIF-8 Nanoparticles

ZIF-8 was prepared by mixing 2-MeIm and Zn(NO₃)₂·6H₂O in methanol: A solution of zinc nitrate in methanol (0.4 mL, 839.55 mM) was added to HEPES buffer (pH 7.4, 5 mL, 3 mM), followed by dropwise addition of 2-MeIm (0.2 mL, 6.09 M) under magnetic stirring at 800 rpm for 10 minutes. The resulting mixture was centrifuged at 15100 g for 5 minutes, washed thrice with methanol, and vacuum dried at 60 °C to yield ZIF-8. For ZIF(Mn) synthesis, HEPES buffer (pH 7.4, 5 mL, 3 mM) was added sequentially to zinc nitrate-methanol (0.4 mL, 839.55 mM) and manganese nitrate-methanol (0.2 mL, 108.86 mM), followed by dropwise addition of 2-MeIm (0.2 mL, 6.09 M) under magnetic stirring for 10 minutes at 800 rpm. The resulting product was centrifuged at 15100 g for 5 minutes, washed thrice with methanol, and vacuum dried at 60 °C to obtain ZIF(Mn).

Synthesis of Baicalin-Loaded Manganese-Doped ZIF-8 Nanoparticles

A solution of zinc nitrate-methanol (0.4 mL, 839.55 mM), manganese nitrate-methanol (0.2 mL, 108.86 mM), and BA (1 mL, 1 mg/mL) was stirred in HEPES buffer (5 mL, 3 mM) at 800 rpm. 2-MeIm (0.2 mL, 6.09 M) was added dropwise and stirred at 800 rpm for 15 minutes. The resulting precipitate was collected by centrifugation, washed thrice with methanol, resuspended in 1 mL of methanol, and added dropwise to manganese nitrate-ethanol (5 mL, 174.19 mM) under stirring for 2 hours at 800 rpm. After centrifugation at 4300 g for 5 minutes, the supernatant was discarded, and BA@ZIF(Mn) was obtained by washing thrice with methanol and vacuum drying at 60 °C.

Synthesis and Encapsulation of Baicalin-Loaded Manganese-Doped ZIF-8 Nanoparticles Modified with Folic Acid and Polyethylene Glycol

Folic acid (56.3 mg) and EDCI (42.925 mg) were dissolved in 25 mL of DMSO and stirred at 35°C for 30 minutes. NHS (28.775 mg) was added and stirred for 3 hours. Then, CH₃O-PEG_{2K}-OH (425 mg, dissolved in 25 mL DMSO) and three drops of TEA were added and stirred at 35 °C for 3 days. The mixture was dialyzed against 50 mL of ddH₂O for one day and lyophilized. The compound was dissolved in 15 mL of DMSO, and lipoic acid (38.65 mg), EDCI (59.875 mg), and DMAP (38.125 mg) were added and stirred at 35 °C for 3 days. The mixture was dialyzed against ddH₂O for 3 days and lyophilized to obtain a yellow flocculent product, methoxy FA-PEG.

FA-PEG was adsorbed onto the surface of pre-formed BA@ZIF(Mn). BA@ZIF(Mn) was dispersed in a 1 mg/mL FA-PEG solution using deionized water as the solvent and stirred at room temperature at 800 rpm for 2 hours to form a BA@ZIF(Mn)/FA-PEG suspension. The pale yellow product was collected by centrifugation at 4300 g for 5 minutes, washed three times with deionized water, and lyophilized to obtain a yellow-brown flocculent product, BA@ZIF(Mn)/FA-PEG.

Physicochemical Characterization

The particle size and Zeta potential of the materials were measured using a nanoparticle size and Zeta potential analyzer (Malvern Zetasizer Nano ZS90, UK) with data acquisition software provided by the instrument. The morphology was observed using a transmission electron microscope (TEM, Thermo Scientific Talos F200X G2, USA), and elemental distribution was determined using energy-dispersive X-ray spectroscopy (EDX) in the same TEM system. FTIR (Thermo Scientific Nicolet iS20, USA) was used to detect organic binding information, confirming the presence of FA-PEG and BA in the ZIF-8 NPs carrier.

To evaluate the stability of BA@ZIF(Mn)/FA-PEG NPs, we measured the changes in diameter and polydispersity index (PDI) of the nanoparticles under different conditions. The nanoparticles were dispersed in two media: PBS (pH=7.4) and serum. Particle size and PDI were monitored over a 7-day period using dynamic light scattering (DLS) to determine the stability of the nanoparticles in these environments.

Drug Loading and Encapsulation Efficiency

To determine the drug loading (DL%) and encapsulation efficiency (EE%) of BA@ZIF(Mn)/FA-PEG, various concentrations of BA@ZIF(Mn)/FA-PEG (30, 35, 40, 45, 50 µg/mL, 1 mL) were centrifuged at 4300 g for 20 minutes. The supernatant was collected and analyzed using a UV spectrophotometer (Model 752, Shanghai Jinghua Instruments, China) at 278 nm to determine the concentration of free BA.²⁴ Encapsulation efficiency (EE%) was calculated based on the concentration of free BA. The precipitate was washed with PBS buffer three times, freeze-dried, and weighed to determine the drug loading (DL%) of BA@ZIF(Mn)/FA-PEG. Drug loading and encapsulation efficiency were calculated using the following formulas:

$$\text{Drug loading (\%)} = (W_t - W_f) / W_n \times 100\%$$

$$\text{Encapsulation efficiency (\%)} = (W_t - W_f) / W_t \times 100\%$$

where W_t is the initial total amount of BA, W_f is the amount of free BA in the supernatant after centrifugation, and W_n is the average weight of the freeze-dried BA@ZIF(Mn)/FA-PEG. All measurements were performed in triplicate.

In vitro Drug Release of Nanoparticles Under Different pH Conditions

The in vitro drug release performance of BA@ZIF(Mn)/FA-PEG was assessed using the dialysis bag method at 37 °C in PBS under varied pH conditions. Initially, standard BA solutions with concentrations ranging from 0 to 128 µg/mL were prepared, and their absorbance at 278 nm was measured using a UV spectrophotometer.²⁵ The drug release profile was subsequently analyzed using Origin 2017 software.

Next, 10 mg of BA@ZIF(Mn)/FA-PEG was placed inside a dialysis bag (molecular weight cutoff: 3500) and immersed in a 50 mL centrifuge tube containing PBS solutions adjusted to pH 7.4, 6.8, or 5.5. The release study was

conducted at 37 °C with magnetic stirring in the dark. Samples (1 mL) were withdrawn at predetermined intervals (0.5, 1, 2, 4, 6, 8, 10, 12, 24, 36, 48 hours), and their absorbance at 278 nm was measured using a UV spectrophotometer to determine BA concentration. The cumulative release percentage (CR%) of BA was calculated, and each experiment was performed in triplicate. To maintain a constant volume, an equal volume of fresh release medium was replenished after each sampling, and the release medium was completely replaced every 24 hours. Use the following equation to calculate the cumulative release percentage (Q) and plot the release curve. Sink conditions remained during the experimental duration.

$$Q = [V_0 C_i + V \sum C_{(i-1)}] / m \times 100\%$$

where m represents the total amount of BA in BA-loaded BA@ZIF(Mn)/FA-PEG nanoparticles inside the dialysis bags, V_0 represents the total volume of release media, C_i represents drug concentration in release medium at time i , Q represents the cumulative release percentage of BA, and V represents the volume of sample per time, respectively.

Hemolysis Assay

Fresh whole blood from mice was centrifuged at 1700 g for 10 minutes to isolate red blood cells (RBCs). The supernatant was discarded, and the RBCs were washed three times with saline before being diluted to a 4% (v/v) RBC suspension with saline. Subsequently, 100 μ L of the diluted RBC suspension was mixed with 1 mL of various concentrations of BA@ZIF(Mn)/FA-PEG NPs solution and incubated at 37 °C for 3 hours. Following incubation, the mixture was centrifuged at 100 g for 3 minutes, and the absorbance of the supernatant at 540 nm was measured using a UV spectrophotometer.

The negative control consisted of saline, whereas Triton X-100 served as the positive control. The hemolysis rate (HR %) was calculated using the formula:

$$\text{Hemolysis Rate (\%)} = (A_s - A_N) / (A_P - A_N) \times 100\%$$

where A_s is the absorbance of the sample containing BA@ZIF(Mn)/FA-PEG, A_N is the absorbance of the negative control (saline), and A_P is the absorbance of the positive control (Triton X-100).

Cellular Uptake

Drug solutions were prepared in serum-free culture medium (Cy5.5/BA@ZIF(Mn) NPs group and Cy5.5/BA@ZIF(Mn)/FA-PEG NPs group, both at a BA concentration of 50 μ g/mL). B16-F10 cells were seeded into 6-well plates and incubated overnight. Upon reaching 70% confluence, cells were treated with the respective drug solutions in serum-free culture medium and incubated at 37 °C for 12 hours. Subsequently, cells were washed three times with PBS and fixed with 4% paraformaldehyde for 15 minutes. DAPI solution (1 μ g/mL) was then applied for 10 minutes in the dark to stain the cells. Cellular localization was examined using an inverted fluorescence microscope (Nexcope NIB620-FL, Ningbo Yongxin Optics Co., Ltd., China).

Cytotoxicity Assay

The cytotoxicity of BA@ZIF(Mn)/FA-PEG NPs against B16-F10 cells was evaluated using the CCK-8 assay. Cells were seeded into 96-well plates at a density of 1.0×10^4 cells per well and cultured overnight at 37 °C with 5% CO₂. Following incubation, 100 μ L of serum-free culture medium containing varying concentrations of samples (BA group, BA@ZIF(Mn) NPs group, and BA@ZIF(Mn)/FA-PEG NPs group) was added to each well in triplicate. After 12 hours of treatment, 10 μ L of CCK-8 solution was added to each well, and the plates were further incubated for 1 hour. The absorbance at 450 nm was measured using a microplate reader (Multiskan FC, Thermo Fisher Scientific Inc., USA).

To assess the biocompatibility of the nanomaterials, a blank nanomaterial group (ZIF(Mn)/FA-PEG) was included. Both cancerous (B16-F10) and normal (L929) cell lines were utilized to evaluate the toxicity of the blank materials. Cell viability (CV%) was calculated using the formula:

$$\text{Cell Viability (\%)} = (A_s - A_b) / (A_c - A_b) \times 100\%$$

where A_s is the OD value of the experimental wells, A_b is the OD value of the blank wells, and A_c is the OD value of the control wells.

Detection of Cell Apoptosis

Cell culture methods were identical to those described in Section Cytotoxicity Assay. After 24 hours of different drugs treatment (PBS group, BA group, BA@ZIF(Mn) NPs group, and BA@ZIF(Mn)/FA-PEG NPs group), cells were stained with Hoechst 33258 for 30 minutes, washed three times with PBS, and observed under an inverted fluorescence microscope to assess nuclear morphology. All procedures were conducted under dark conditions. Additionally, cells were trypsinized, dispersed into single cells, and stained using the FITC Annexin V Apoptosis Detection Kit I following the manufacturer's protocol. FITC Annexin V and PI-labeled cells were quantified using a flow cytometer (FACS Aria III, BD Biosciences, USA), with data analysis performed using FlowJo V10 software (FlowJo LLC, Ashland, OR, USA).

Detection of Reactive Oxygen Species and Lipid Peroxidation in Cells

Experimental groups and cell culture methods followed those outlined in Section *Detection of Cell Apoptosis*. Following the Reactive Oxygen Species (ROS) Assay Kit protocol, each well received 2 mL of 2',7'-dichlorodihydrofluorescein diacetate (DCFH-DA, 10 $\mu\text{mol/L}$) and was incubated at 37 °C for 20 minutes. Following washing, fluorescence signals in B16-F10 cells were visualized using an inverted fluorescence microscope. Furthermore, cells from each group were sonicated in an ice bath and centrifuged at 1700 g for 5 minutes to obtain supernatants. The MDA content in cells was quantified using the thiobarbituric acid method, strictly adhering to kit instructions.

Real-Time PCR Detection of Ferroptosis-Related Gene Expression

Experimental conditions and cell culture procedures mirrored those described in Section *Detection of Cell Apoptosis*. Total RNA was extracted using the Trizol Plus RNA Purification Kit, and its concentration was determined using a micro-UV-visible spectrophotometer (NanoDrop 2000, Thermo Fisher Scientific Inc., USA) to ensure an A260/A280 ratio between 1.7 and 2.0. First-strand cDNA was synthesized using M-MLV reverse transcriptase. Real-time PCR (FQD-96C, Hangzhou Bioer Technology Co., Ltd, China) was employed to quantify the expression levels of ferroptosis-related genes, including GPX4, FTH1, PTGS2, and ACSL4. The $2^{-\Delta\Delta C_t}$ method was utilized to calculate relative gene expression levels. Primers were synthesized by Sangon Biotech (Shanghai, China), with sequences listed in Table 1.^{26–28}

Western Blot Analysis

Western blotting was performed to assess the expression of folate receptors in B16-F10 cells and tumor tissues, as well as to analyze proteins associated with ferroptosis, including GPX4, FTH1, PTGS2, and ACSL4. B16-F10 cells were lysed using RIPA lysis buffer containing 1 mM phenylmethanesulfonyl fluoride (PMSF) to inhibit protease activity, while tumor tissues were homogenized in the same buffer. Total protein concentrations were determined using a BCA Protein Assay Kit according to the manufacturer's instructions. For SDS-polyacrylamide gel electrophoresis (SDS-PAGE), 20 μg of protein from each sample was mixed with loading buffer, denatured, and separated on the gel. The proteins were then

Table 1 Primer Sequences for Real-Time PCR

Gene	Forward primer (5'-3')	Reverse primer (5'-3')
GAPDH	AGGTCGGTGTGAACGGATTTG	TGTAGACCATGTAGTTGAGGTCA
GPX4	CAGGAGCCAGGAAGTAAT	CAGCCGTTCTTATCAATGAG
FTH1	TGCCTCCTACGCTATCTGTC	GTCATCACGGTCTGGTTTCTTT
PTGS2	TTCAACACACTCTATCACTGGC	AGAAGCGTTTGCGGTACTCAT
ACSL4	TGAACGTATCCCTGGACTAGG	TCAGACAGTGAAGGGGTGAA

transferred onto polyvinylidene fluoride (PVDF) membranes using a wet transfer system. Membranes were blocked with tris-buffered saline containing 0.1% Tween-20 (TBST) and 5% skim milk powder for 2 hours at room temperature to prevent non-specific binding.

Following blocking, membranes were incubated overnight at 4 °C with primary antibodies specific to the target proteins, diluted 1:1000. After extensive washing with TBST, membranes were incubated with horseradish peroxidase (HRP)-conjugated secondary antibodies, diluted 1:10000, for 1 hour at room temperature. After additional TBST washes, protein bands were visualized using ECL reagents. Chemiluminescent signals were captured using the Tanon-410 automatic gel imaging system (Shanghai Tianneng Corporation, China).

MR Imaging

BA@ZIF(Mn)/FA-PEG NPs at different concentrations were dispersed in deionized water, and T1-weighted imaging was conducted using a 3.0T MRI scanner (GE Signa, USA). C57BL/6J Nifdc mice bearing subcutaneous B16-F10 melanoma xenografts were used as animal models. The mice received a tail vein injection of BA@ZIF(Mn)/FA-PEG NPs suspension (2 mg·kg⁻¹). T1-weighted MR scans of the animals were performed using a dedicated small animal imaging coil before injection and 6 hours post-injection.

In vivo Tumor Inhibition Study

A subcutaneous xenograft tumor model was established by injecting 1×10⁶ B16-F10 cells into the backs of C57BL/6J Nifdc mice. The mice were randomly divided into five groups: PBS, ZIF(Mn)/FA-PEG NPs, BA, BA@ZIF(Mn) NPs, and BA@ZIF(Mn)/FA-PEG NPs (BA dose: 2 mg·kg⁻¹). Treatments were administered via tail vein injection every 2 days for 14 days (7 injections total).

Throughout the treatment period, body weight and tumor volume were measured and recorded every 2 days. At the end of the study, mice were euthanized, and tumors and organs were harvested for histopathological analysis using H&E staining. Tumor weights were recorded and photographed for visual documentation.

Tumor growth inhibition (TGI) was calculated using the following formula:

$$\text{TGI} = (1 - W_t/W_c) \times 100\%$$

where W_t is the mean tumor weight of treatment group, and W_c is the mean tumor weight of control group.

Immunohistochemistry and TUNEL Staining of Tumor Tissue

Tumor tissues from each experimental group were fixed in 4% neutral formaldehyde, dehydrated, paraffin-embedded, and sectioned at 4 μm thickness. Deparaffinization was followed by antigen retrieval using EDTA buffer (pH 8.0). Sections were blocked with 1:20 diluted goat serum and incubated overnight at 4°C with primary antibodies. After washing with PBS, sections were incubated with appropriate secondary antibodies, developed using DAB substrate, counterstained with hematoxylin, dehydrated, and mounted, strictly adhering to kit instructions. Analysis was performed using an optical microscope (Olympus CX43, Olympus Corporation, Japan).

For TUNEL staining, deparaffinized sections were treated with proteinase K (20 μg/mL) at 37 °C for 30 minutes. Subsequent steps included incubation with 3% hydrogen peroxide, TUNEL reaction mixture incubation at 37 °C for 60 minutes in the dark, followed by incubation with Streptavidin-HRP and DAB solution for color development. Counterstaining was done with hematoxylin, followed by dehydration and mounting. Sections were observed under an optical microscope.

Statistical Analysis

Statistical analyses were conducted using SPSS 26.0 software (IBM Corp., Armonk, NY, USA). Data were presented as mean ± standard deviation (mean ± SD). Parametric tests such as Student's *t*-test or one-way ANOVA were employed for normally distributed data, while non-parametric analyses like the Kruskal–Wallis *H*-test were used for non-normally distributed data. A significance level of $p < 0.05$ was considered statistically significant ($*p < 0.05$, $**p < 0.01$, $***p < 0.001$).

Results and Discussion

Preparation and Characterization of BA@ZIF(Mn)/FA-PEG NPs

The preparation strategy for BA@ZIF(Mn)/FA-PEG nanocomposites is illustrated in Figure 1. We characterized the samples (ZIF(Mn), BA@ZIF(Mn), ZIF(Mn)/FA-PEG, and BA@ZIF(Mn)/FA-PEG) using DLS and transmission electron microscopy (TEM). TEM images revealed that ZIF(Mn), ZIF(Mn)/FA-PEG, and BA@ZIF(Mn)/FA-PEG NPs exhibit a regular hexahedral structure (Figure 2). The crystallization kinetics of ZIF-8 indicate a significant influence of pH.^{29,30} In our study, the addition of BA and Mn^{2+} adjusted the solution pH from 7.2~7.4 to 6.5~6.8, facilitating ZIF-8 crystallization. Consequently, ZIF(Mn) and BA@ZIF(Mn) display more regular structures compared to ZIF-8 (Figures 2A–C). FA-PEG modification resulted in smoother edges of ZIF(Mn) NPs, appearing as a transparent film coating with minor mechanical adsorption of FA-PEG particles visible on the surface (Figure 2D). Furthermore, BA@ZIF(Mn)/FA-PEG NPs exhibited improved dispersion compared to ZIF(Mn) and BA@ZIF(Mn) NPs (Figure 2E and F), indicating that FA-PEG modification prevents aggregation without altering the inherent structure of ZIF(Mn) and BA@ZIF(Mn) NPs. The elemental distribution of ZIF(Mn) was characterized via EDS-elemental mapping (Figure 2G). The desired elements, namely C (red), O (blue), N (green), Zn (cyan), and Mn (fuchsia), were found to be homogeneously distributed throughout the ZIF. This confirms the uniform dispersion of Mn within the ZIF matrix.

DLS results indicated the size and distribution of the samples studied (Figure 3A–D). The average diameter of BA@ZIF(Mn)/FA-PEG was 184.47 nm (PDI: 0.263), consistent with TEM observations. Before and after FA-PEG modification, the zeta potentials of ZIF(Mn) and BA@ZIF(Mn) shifted from positive (10.28±1.01 mV and 6.34±0.67 mV, respectively) to negative (−4.22±0.45 mV and −2.42±0.58 mV, respectively) (Figure 3E). This shift is attributed to successful FA-PEG modification, introducing negatively charged carboxyl ions in the aqueous solution. Prior studies

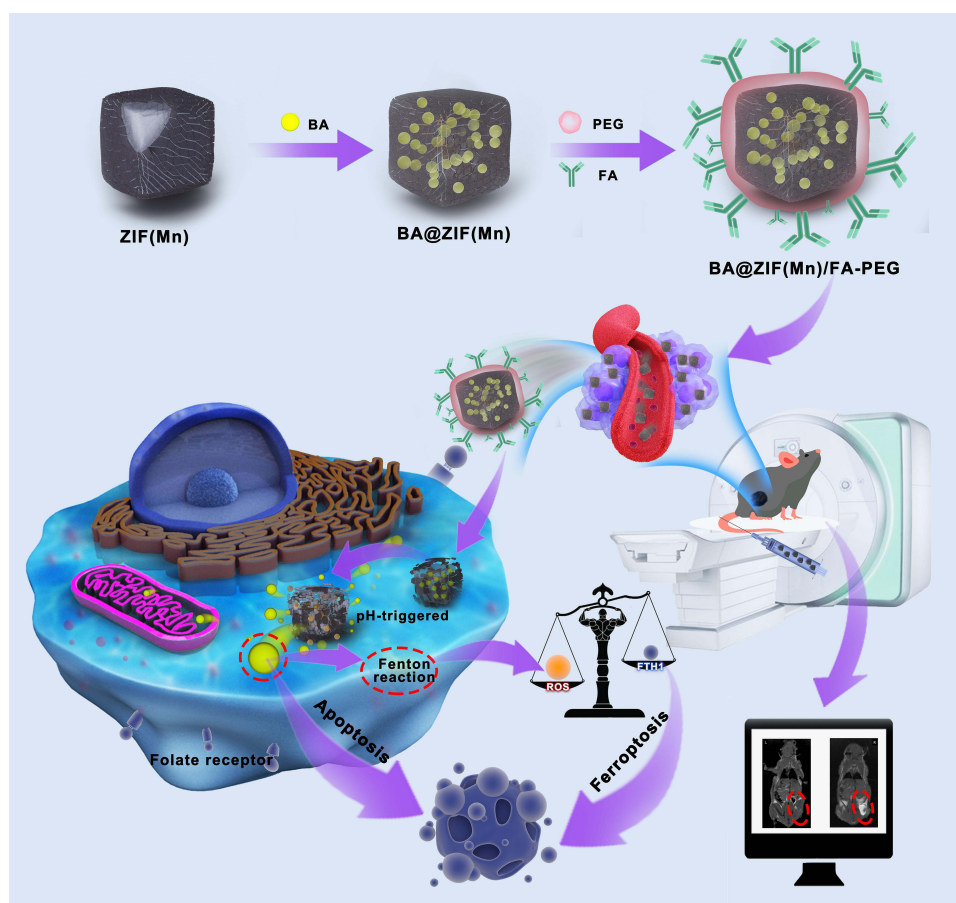


Figure 1 Schematic illustration of the preparation of BA@ZIF(Mn)/FA-PEG NPs and their use in imaging-guided, targeted induction of apoptosis and ferroptosis.

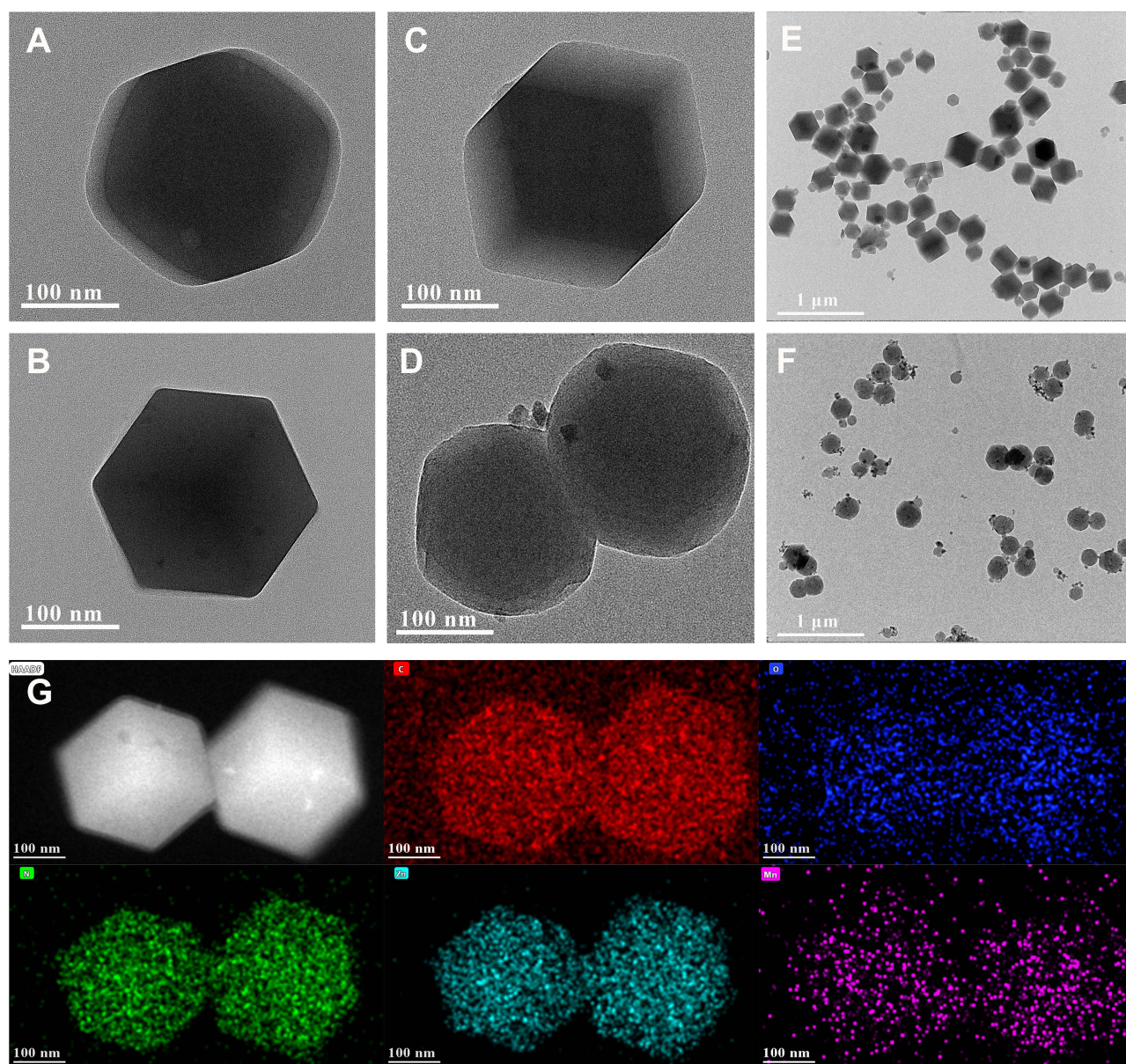


Figure 2 TEM images of (A) ZIF, (B) ZIF(Mn), (C) BA@ZIF(Mn), and (D) BA@ZIF(Mn)/FA-PEG, with scale bars of 100 nm; additional TEM images of (E) BA@ZIF(Mn) and (F) BA@ZIF(Mn)/FA-PEG, with scale bars of 1 μm. (G) Elemental distribution in ZIF(Mn) characterized by EDS-elemental mapping, showing homogeneous distribution of the desired elements: C (red), O (blue), N (green), Zn (cyan), and Mn (fuchsia). Scale bar = 100 nm.

have demonstrated that negatively charged nanomaterials reduce plasma protein adsorption, prolonging circulation time and enhancing drug accumulation at tumor sites via the enhanced permeability and retention (EPR) effect.^{31–33} Additionally, FA-PEG modification acts as a surface-targeting ligand facilitating cellular internalization and enhancing in vitro circulation by reducing uptake by non-Kupffer cells in the liver.³⁴

To further confirm the successful preparation of BA@ZIF(Mn)/FA-PEG NPs, we analyzed the Fourier-transform infrared (FTIR) spectra of BA, FA-PEG, ZIF(Mn), and BA@ZIF(Mn)/FA-PEG (Figure 3F). In the spectrum of BA@ZIF(Mn)/FA-PEG, characteristic peaks of BA at 1726 cm^{-1} (carbonyl stretching vibration of uronic acid), 1608 cm^{-1} , 1572 cm^{-1} , and 1493 cm^{-1} (skeletal C=C stretching vibrations) disappeared, aligning closely with the peaks of ZIF(Mn). This suggests that BA absorption peaks overlapped with ZIF(Mn) due to physical shielding. Additionally, BA@ZIF(Mn)/FA-PEG exhibited characteristic peaks of FA-PEG at 3436 cm^{-1} ν (O-H), 2884 cm^{-1} ν (-

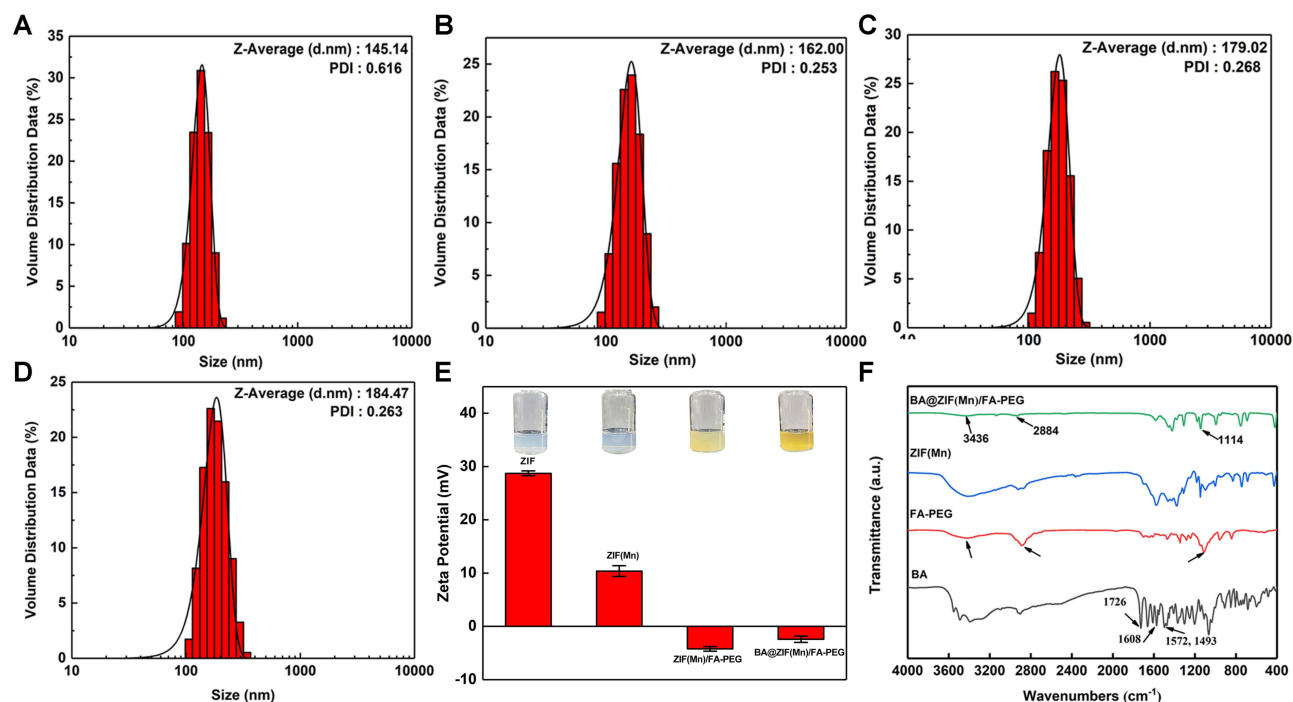


Figure 3 (A-D) Size distributions of ZIF-8 NPs, ZIF(Mn) NPs, ZIF(Mn)/FA-PEG NPs, and BA@ZIF(Mn)/FA-PEG NPs, as determined by DLS measurements. **(E)** Zeta potential measurements for ZIF NPs, ZIF(Mn) NPs, ZIF(Mn)/FA-PEG NPs, and BA@ZIF(Mn)/FA-PEG NPs. **(F)** FTIR spectra of BA, FA-PEG, ZIF(Mn), and BA@ZIF(Mn)/FA-PEG. Data are presented as mean \pm SD, $n = 3$.

CH₂), and 1114 cm⁻¹ (C-O-C), with no new peaks identified, confirming the attachment of FA-PEG molecules to BA@ZIF(Mn).

The stability analysis revealed that the BA@ZIF(Mn)/FA-PEG NPs exhibited no significant changes in particle size or PDI over the 7-day storage period in PBS (pH=7.4) or serum, indicating excellent stability in these environments (Figure S1). These findings confirm that the nanoparticles maintain their structural integrity in aqueous and physiological conditions, which is crucial for ensuring their reliable performance in drug delivery applications. The consistent diameter and PDI across different solutions further highlight the robustness of the nanoparticle system, suggesting its potential for stable in vivo application without aggregation or instability. The stability of the nanoparticles under physiological conditions is essential for minimizing off-target effects and ensuring sustained therapeutic efficacy, which is important for the successful clinical translation of the BA@ZIF(Mn)/FA-PEG NPs.

Loading and Release

This study evaluated the loading and release behavior of BA from ZIF(Mn)/FA-PEG. Table 2 presents the results of drug loading capacity (DLC) and encapsulation efficiency (EE). With DLC for BA measured at 33.50 \pm 0.04% and EE at 71.34 \pm 0.02%, BA@ZIF(Mn)/FA-PEG NPs demonstrate higher drug loading and encapsulation efficiencies compared to other BA nanodelivery systems.^{25,35}

Drug release experiments were conducted in PBS buffers with different pH values (7.4, 6.8, and 5.5), mimicking normal tissue, tumor, and lysosomal microenvironments, respectively.³⁶ As illustrated in Figure 4, BA@ZIF(Mn)/FA-PEG NPs exhibited distinct pH-responsive release profiles of BA in PBS buffers at different pH values, with accelerated release observed in acidic conditions. Under pH 7.4 conditions, only 33.24 \pm 0.42% of BA was released from the drug carrier within 12 hours, indicating low release rates in normal tissue microenvironments such as blood, thereby ensuring efficient accumulation and release in tumor tissues. At pH 6.8 and 5.5, the 12-hour cumulative releases of BA increased to 36.37 \pm 0.40% and 43.69 \pm 1.27%, respectively, confirming the faster release of BA in acidic environments. This pH-responsive behavior of BA@ZIF(Mn)/FA-PEG NPs can be attributed to the cleavage of metal ion-ligand coordination bonds (Zn²⁺ with nitrogen atoms from meIm⁻) under acidic conditions. Protonation of the ligand in acidic environments

Table 2 Results of Drug Loading and Entrapment Efficiency (Mean \pm SD, n =3)

Concentration of BA ($\mu\text{g/mL}$)	Drug loading (%)	Encapsulation efficiency (%)
10	4.96 \pm 0.01	94.44 \pm 0.01
20	7.53 \pm 0.01	86.08 \pm 0.03
30	11.10 \pm 0.01	84.58 \pm 0.02
40	17.84 \pm 0.02	81.57 \pm 0.03
50	33.50 \pm 0.04	71.34 \pm 0.02
60	29.87 \pm 0.07	73.57 \pm 0.10

induces bond dissociation, leading to ZIF(Mn) disintegration and the accelerated release of BA.^{29,37} Consequently, BA@ZIF(Mn)/FA-PEG NPs serve as pH-triggered drug carriers, enhancing the cytotoxicity of the drug-loaded nano-carrier system against cancer cells while minimizing adverse effects.

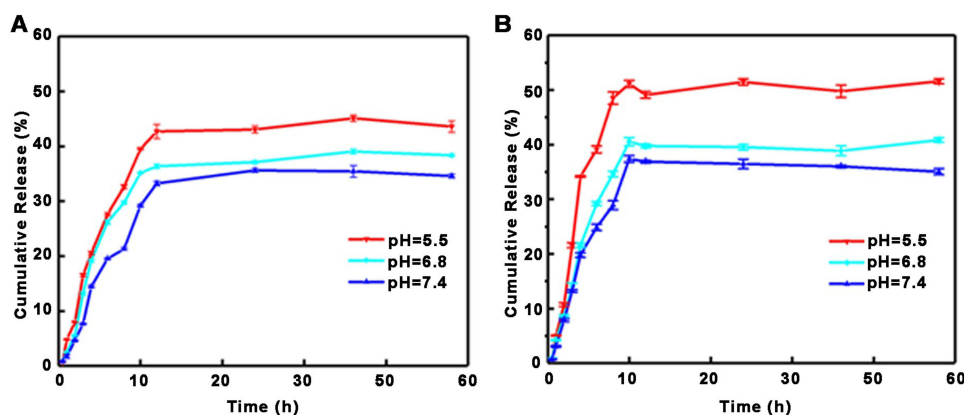
Biocompatibility

Ensuring minimal hemolysis when introducing non-biological substances into the body is critical. Biomaterials are categorized based on hemolytic activity: non-hemolytic (0~2% hemolysis), slightly hemolytic (2~5% hemolysis), and hemolytic (>5% hemolysis).³⁸ As depicted in Figure 5, increasing concentrations of BA@ZIF(Mn)/FA-PEG NPs in a 96-well plate resulted in some hemolysis, yet the rate remained below 20 \pm 1.57%. At the half-maximal inhibitory concentration (IC₅₀) of 50 $\mu\text{g/mL}$ for BA@ZIF(Mn)/FA-PEG NPs, the hemolytic activity was measured at 4.41 \pm 0.74%, indicating excellent biocompatibility of the material.

Cellular Uptake

The uptake behavior of BA@ZIF(Mn)/FA-PEG NPs in B16-F10 cells was investigated using fluorescence imaging (Figure 6A). The Cy5.5/BA@ZIF(Mn)/FA-PEG NPs group exhibited significantly higher fluorescence intensity compared to other groups, indicating efficient targeting and internalization in B16-F10 cells. Western blot analysis confirmed the expression of β -folate receptors (β -FR) on both B16-F10 cells and tumor tissues, validating β -FR as a molecular target for BA@ZIF(Mn)/FA-PEG NPs (Figure S2). Furthermore, data retrieved from the Human Protein Atlas (HPA) corroborated the expression of folate receptor 2 (FOLR2) in human melanoma tissues, providing additional support for the applicability of folate receptor-targeted therapies across species.³⁹ The presence of β -FR facilitates folate receptor-mediated endocytosis, significantly enhancing nanoparticle uptake in melanoma cells.

The FA-PEG modification not only improves biocompatibility and prolongs circulation time but also facilitates precise and stable active targeting to tumor cells through folate receptor interactions. In addition, BA@ZIF(Mn)/FA-PEG

**Figure 4** Drug release kinetics from BA@ZIF(Mn) (A) and BA@ZIF(Mn)/FA-PEG (B) in PBS buffer solutions at pH 5.5, 6.8, and 7.4. Data are presented as mean \pm SD, n = 3.

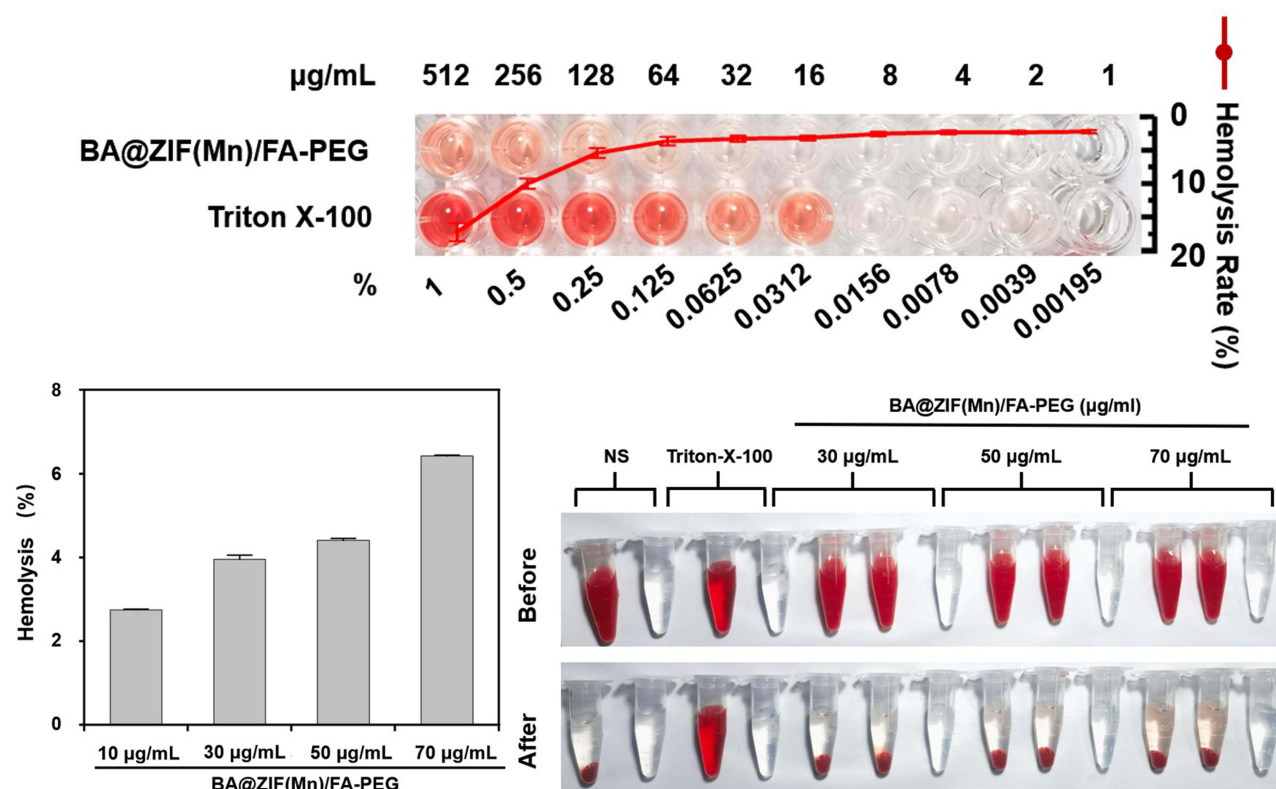


Figure 5 Hemolysis assay of BA@ZIF(Mn)/FA-PEG NPs in vitro. Relative viabilities of B16-F10 cells after incubation with various concentrations of blank ZIF(Mn)/FA-PEG NPs for 24 hours. Results are presented as mean \pm SD, n = 3.

NPs exploit pH-responsive mechanisms and the EPR effect to achieve effective passive targeting, resulting in preferential accumulation in tumor tissues.^{36,40} This dual-targeting strategy underscores the therapeutic potential of BA@ZIF(Mn)/FA-PEG NPs in treating melanoma.

Cytotoxicity

In the experimental dose range, BA@ZIF(Mn)/FA-PEG exhibited no significant cytotoxicity to B16-F10 and L929 cells (Figure 6B). Conversely, BA@ZIF(Mn)/FA-PEG demonstrated dose-dependent antiproliferative effects on B16-F10 cells (Figure 6C). At a concentration of 50 μ g/mL, BA@ZIF(Mn)/FA-PEG NPs significantly reduced cell viability compared to BA and BA@ZIF(Mn) groups under identical conditions, highlighting enhanced intracellular delivery of BA facilitated by BA@ZIF(Mn)/FA-PEG NPs. Consequently, subsequent experiments were conducted at this concentration, where BA@ZIF(Mn)/FA-PEG NPs achieved IC₅₀ (the half maximal inhibitory concentration) for B16-F10 cells.

Induction of Apoptosis

Apoptosis, or programmed cell death, is characterized by distinct morphological and biochemical changes, including chromatin condensation, DNA fragmentation, and caspase activation.^{41,42} Inducing apoptosis is a fundamental strategy in cancer therapy, offering a targeted approach to eliminating malignant cells while minimizing damage to healthy tissues.⁴³ BA has demonstrated anticancer effects by inhibiting the proliferation and migration of tumor cells, including breast, lung, liver, and kidney cancers, through apoptosis induction and cell cycle arrest.^{8,44–46} The apoptotic efficacy of BA@ZIF(Mn)/FA-PEG NPs in melanoma cells was evaluated through Hoechst 33258 staining and flow cytometry.

Hoechst 33258 staining revealed significantly more chromatin fragmentation and peripheral nuclear condensation in the BA@ZIF(Mn)/FA-PEG NP-treated group compared to other treatments (Figure 7A), indicative of advanced apoptosis. Flow cytometry further quantified these effects, showing significant induction of early apoptosis (9.19%) and late apoptosis (37.1%) (Figure 7B). These results underscore the potent ability of BA@ZIF(Mn)/FA-PEG NPs to induce

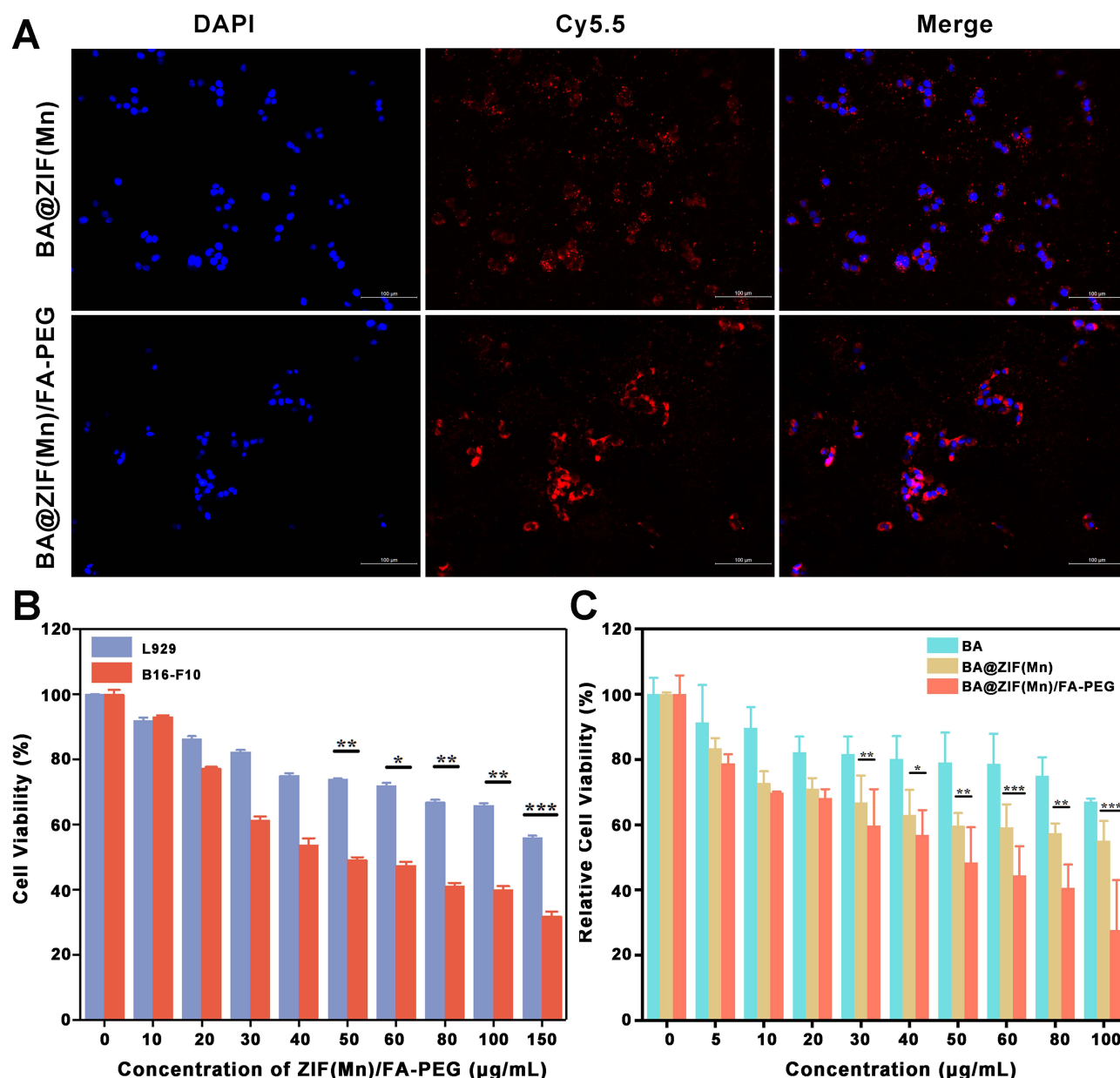


Figure 6 (A) Cellular uptake of Cy5.5/BA@ZIF(Mn) and Cy5.5/BA@ZIF(Mn)/FA-PEG in B16-F10 cells; scale bars are 100 μm. (B) Relative viabilities of B16-F10 cells and L929 cells after being incubated with various concentrations of ZIF(Mn)/FA-PEG NPs for 24 hours. (C) Relative B16-F10 cell viability after incubation with different samples containing equivalent amounts of BA for 12 hours. Data are mean ± SD (n = 3; *p < 0.05; **p < 0.01; ***p < 0.001).

apoptosis in B16-F10 melanoma cells, outperforming BA and BA@ZIF(Mn) alone. This enhanced effect is likely due to the active targeting and improved cellular uptake of BA facilitated by the FA-PEG modification of the NPs.

Previous studies have demonstrated that BA-induced apoptosis is associated with the mitochondrial (intrinsic) apoptotic pathway. Based on these findings, we hypothesize that the apoptosis induced by BA@ZIF(Mn)/FA-PEG NPs may also involve the mitochondrial apoptotic pathway. This pathway is characterized by mitochondrial membrane potential disruption, cytochrome c release, and the sequential activation of caspase-9 and caspase-3, ultimately leading to cell death. BA has been shown to promote mitochondrial dysfunction and caspase activation in other cancer models.^{47–49} While the extrinsic apoptotic pathway, initiated by death receptor activation, could also contribute, it may play a lesser role in this context. Future research will aim to experimentally confirm these mechanisms using caspase activity assays

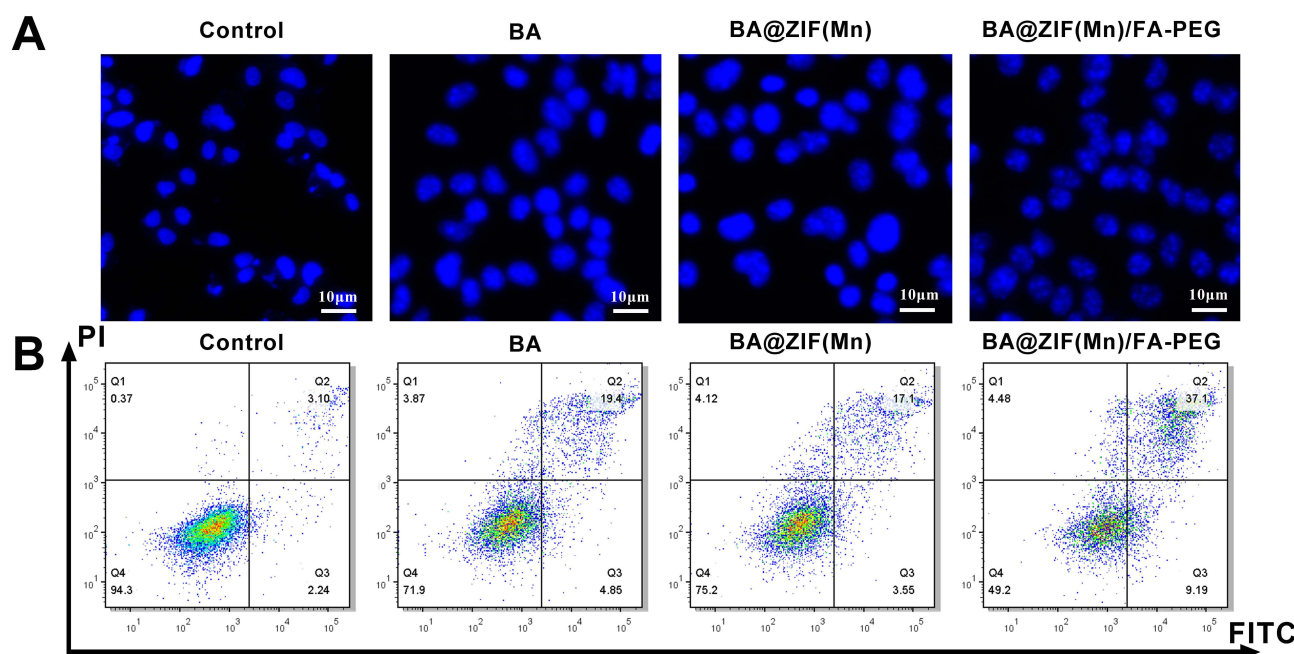


Figure 7 (A) Apoptosis in B16-F10 cells treated with PBS, BA, BA@ZIF(Mn) NPs, and BA@ZIF(Mn)/FA-PEG NPs, observed using an inverted fluorescence microscope with Hoechst 33258 staining; scale bars are 10 μm. **(B)** Apoptosis rates of B16-F10 cells determined by flow cytometry after treatment with PBS, BA, BA@ZIF(Mn), and BA@ZIF(Mn)/FA-PEG.

and mitochondrial analyses, providing a clearer understanding of the apoptotic pathways activated by BA@ZIF(Mn)/FA-PEG NPs.

Induction of Ferroptosis

Recent studies have highlighted BA as a potential inducer of ferroptosis,^{7,8} but its role in melanoma remains poorly understood. Ferroptosis, a form of regulated cell death characterized by iron-dependent lipid peroxidation, has emerged as a critical mechanism in cancer therapy. It is distinct from apoptosis and necrosis and is induced by the accumulation of ROS and lipid peroxides, which lead to cellular damage. This mechanism has gained attention for its therapeutic potential in cancer treatment, as it provides an alternative pathway for killing tumor cells that are resistant to traditional therapies. In this study, we demonstrate that BA and BA@ZIF(Mn)/FA-PEG NPs significantly induce ferroptosis in B16-F10 melanoma cells, as evidenced by elevated ROS levels (Figure 8A and B) and increased MDA content (Figure 8C). To further validate ferroptosis induction, we assessed the expression of ferroptosis-related genes (ACSL4, PTGS2, FTH1, and GPX4) at the mRNA level (Figures 9A–D) and confirmed these findings at the protein level using Western blot analysis (Figure 9E).

Quantitative RT-PCR analysis revealed that BA treatment led to a significant upregulation of ACSL4 and PTGS2 expression, while concurrently downregulating FTH1 and GPX4 compared to the control group. Notably, the BA@ZIF(Mn)/FA-PEG NP treatment group exhibited the most pronounced effects, with further upregulation of ACSL4 and PTGS2, and a more substantial downregulation of FTH1 and GPX4, indicating a stronger ferroptosis-inducing effect of the nanoparticle system compared to free BA. Western blot analysis further corroborated these findings, showing consistent increases in ACSL4 and PTGS2 protein levels, and marked reductions in FTH1 and GPX4 in response to treatment of BA@ZIF(Mn)/FA-PEG NPs. These protein-level changes correlate with increased lipid peroxidation and decreased ferroptosis inhibition. Tubulin was used as a loading control to ensure the reliability of the results.

Taken together, our findings confirm that BA induces ferroptosis in B16-F10 melanoma cells by modulating key ferroptosis markers. The encapsulation of BA in ZIF(Mn)/FA-PEG NPs enhances this effect, likely due to the

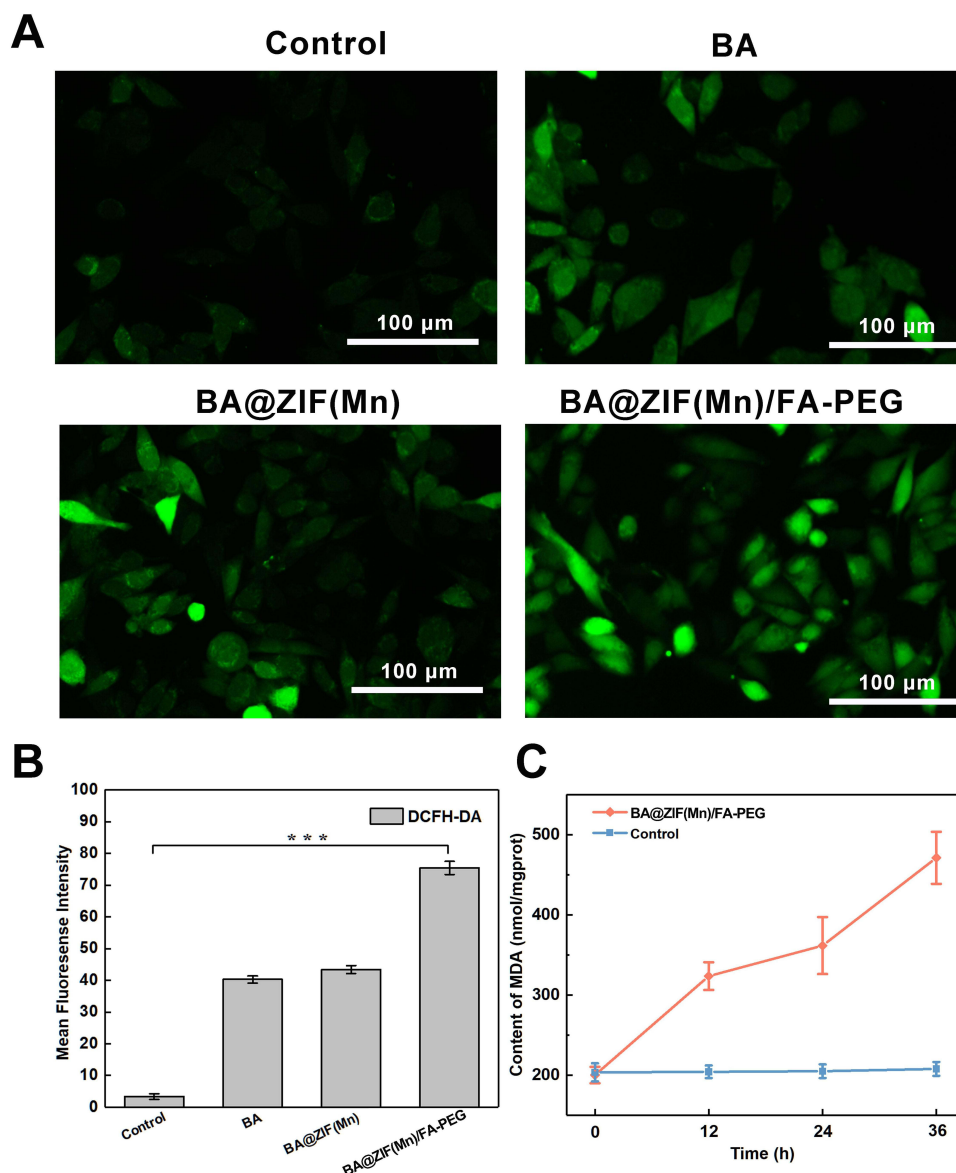


Figure 8 Intracellular ROS content in B16-F10 cells after treatment with PBS, BA, BA@ZIF(Mn), and BA@ZIF(Mn)/FA-PEG. **(A)** DCFH-DA fluorescence imaging showing ROS levels in treated B16-F10 cells; scale bars are 100 μm . **(B)** Quantification of DCFH-DA fluorescence from **(A–C)** Intracellular lipid peroxidation levels measured as relative malondialdehyde (MDA) content at 0, 12, 24 and 36 hours post-treatment with PBS, BA, BA@ZIF(Mn), and BA@ZIF(Mn)/FA-PEG. Data are mean \pm SD ($n = 3$; *** $p < 0.001$).

nanoparticles' synergistic properties, such as efficient drug delivery, pH-responsive release, and targeted tumor accumulation through folate receptor interaction.

MR Imaging

Manganese ion (Mn^{2+}) is a safe contrast agent for MRI due to its high resolution, good contrast, multi-directional imaging capabilities, and non-radioactivity.^{5,50} However, its prolonged examination time and low sensitivity of MRI limits its clinical utility.^{51–53} By incorporating Mn^{2+} into ZIF-8 nanocomposites and leveraging their pH responsiveness, combined with FA-PEG modification, NPs can precisely accumulate in tumor tissues, facilitating targeted drug release and overcoming this limitation. BA@ZIF(Mn)/FA-PEG exhibited a significant concentration-dependent brightening effect in T1-weighted MRI (Figure 10A). The longitudinal relaxivity coefficient (r_1) of BA@ZIF(Mn)/FA-PEG NPs was $13.11 \text{ mM}^{-1}\text{s}^{-1}$, which is three times higher than that of Gd-DTPA ($4.40 \text{ mM}^{-1}\text{s}^{-1}$) (Figure 10B).^{54,55} In vivo MR imaging was conducted on mice bearing B16-F10 tumors injected with BA@ZIF(Mn)/FA-PEG via the tail vein, followed

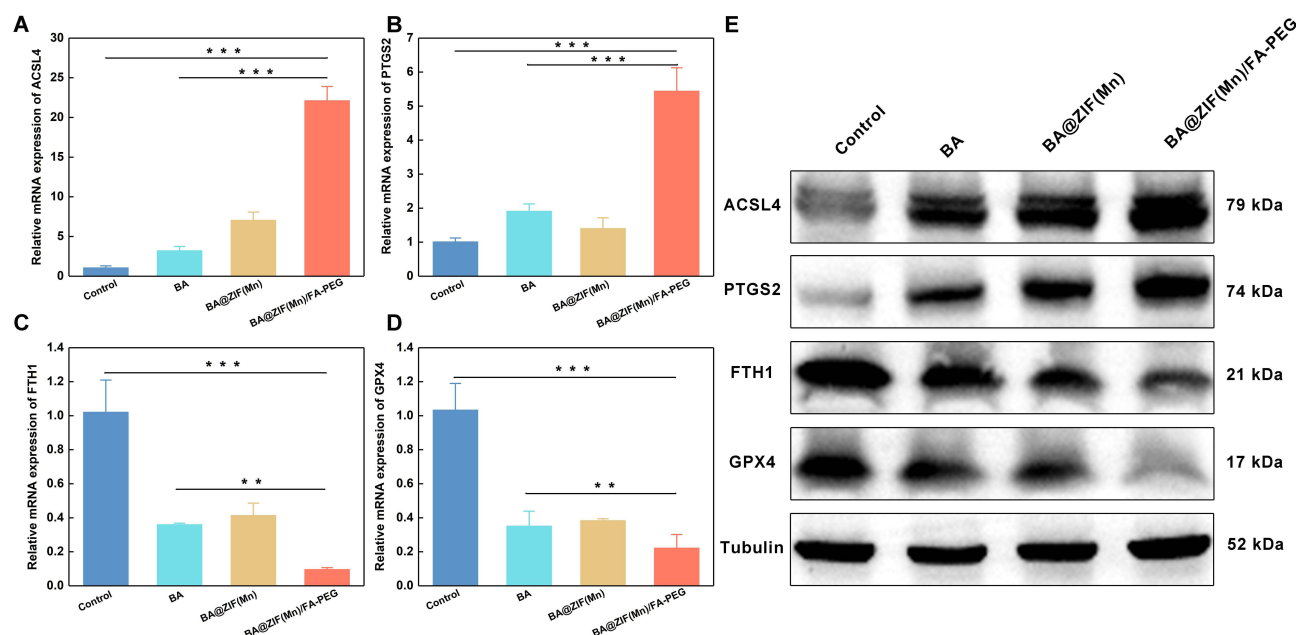


Figure 9 mRNA expression levels of (A) ACSL4, (B) PTGS2, (C) FTH1, and (D) GPX4 in B16-F10 cells following treatment with PBS, BA, BA@ZIF(Mn), and BA@ZIF(Mn)/FA-PEG. Gene expression was assessed by quantitative RT-PCR, and results are presented as relative mRNA expression compared to the control group. (E) Western blot analysis of protein expression levels for ACSL4, PTGS2, FTH1, and GPX4 in B16-F10 cells treated with the same conditions. Tubulin was used as a loading control. Data are mean \pm SD ($n = 3$; $**p < 0.01$; $***p < 0.001$).

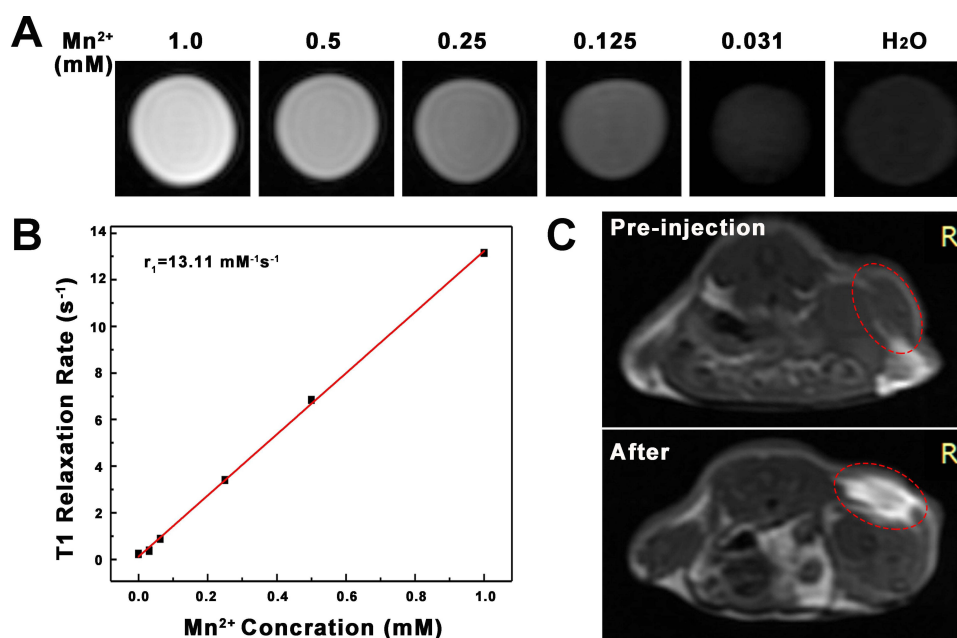


Figure 10 MR Imaging. (A) T1-weighted MR images of BA@ZIF(Mn)/FA-PEG NPs at varying Mn^{2+} concentrations. (B) T1 relaxation rates of aqueous solutions containing BA@ZIF(Mn)/FA-PEG NPs at different Mn^{2+} concentrations. (C) In vivo T1-weighted MR images of a mouse before injection (top) and 6 hours post intravenous injection (bottom) of BA@ZIF(Mn)/FA-PEG NPs.

by imaging with a 3.0T MR system. Post-injection images showed a significant brightening effect in the tumor area (red circle) 6 hours later compared to pre-injection images (Figure 10C), confirming the specificity of the drug delivery system and its tumor accumulation. These results highlight BA@ZIF(Mn)/FA-PEG NPs as an effective MRI-guided drug delivery system for tumor treatment.

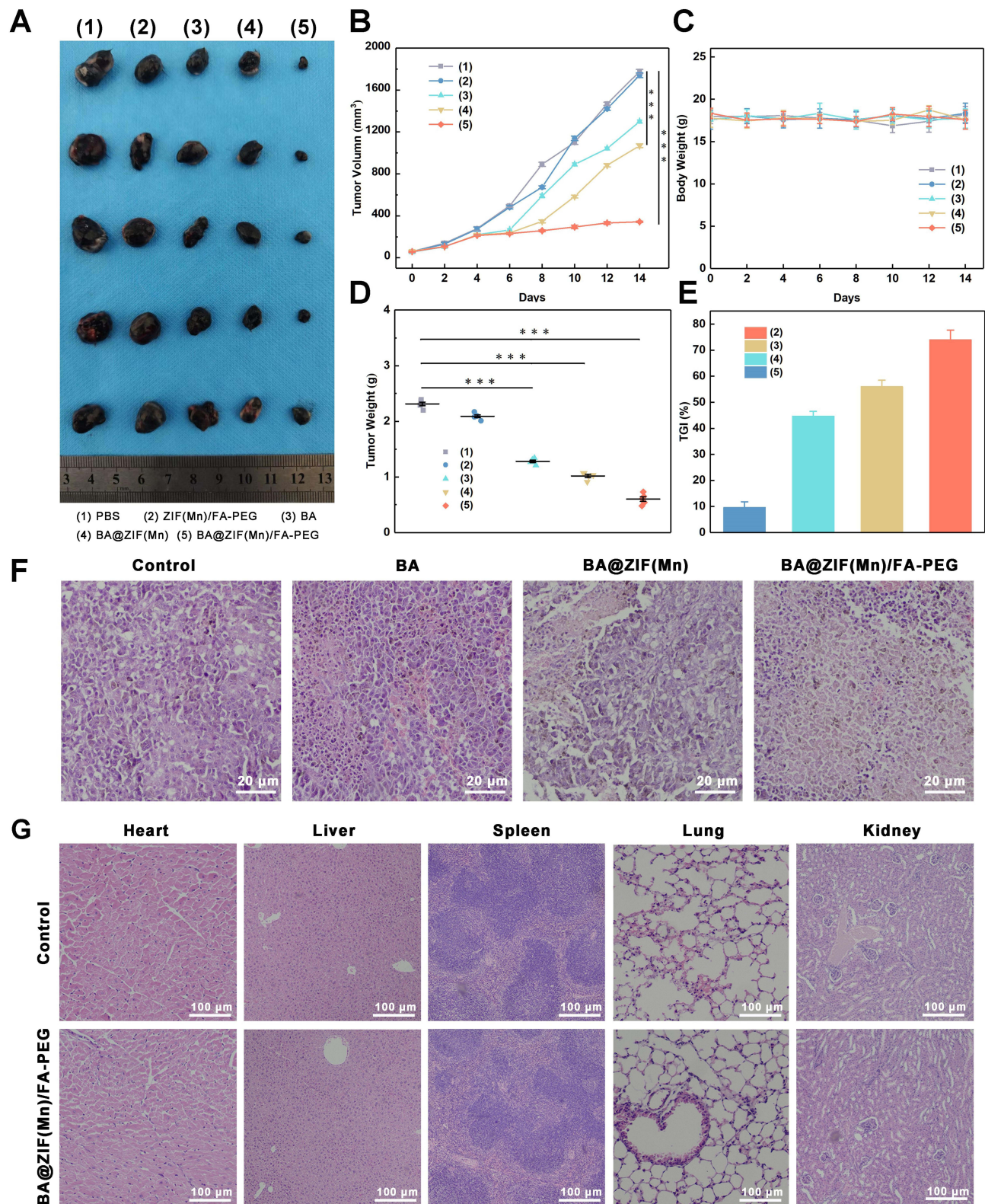


Figure 11 In Vivo Characterization. **(A)** Photographs of tumor samples from each treatment group. Mice were injected via the tail vein with: (1) PBS; (2) ZIF(Mn)/FA-PEG NPs; (3) BA; (4) BA@ZIF(Mn) NPs; or (5) BA@ZIF(Mn)/FA-PEG NPs. Each group comprised five mice. **(B)** Analysis of tumor volume for each group. Photographs of **(C)** body and **(D)** excised tumors weight of tumor-bearing mice following different treatments over 14 days. **(E)** Tumor growth inhibition (TGI) rates for each group after treatment. **(F)** H&E-stained images of tumor sections from different treatment groups after 14 days. Scale bar = 20 μ m. **(G)** H&E-stained images of heart, liver, spleen, lung, and kidney tissues collected from mice after 14 days of treatment. Scale bar = 100 μ m. Data are mean \pm SD ($n = 3$; *** $p < 0.001$).

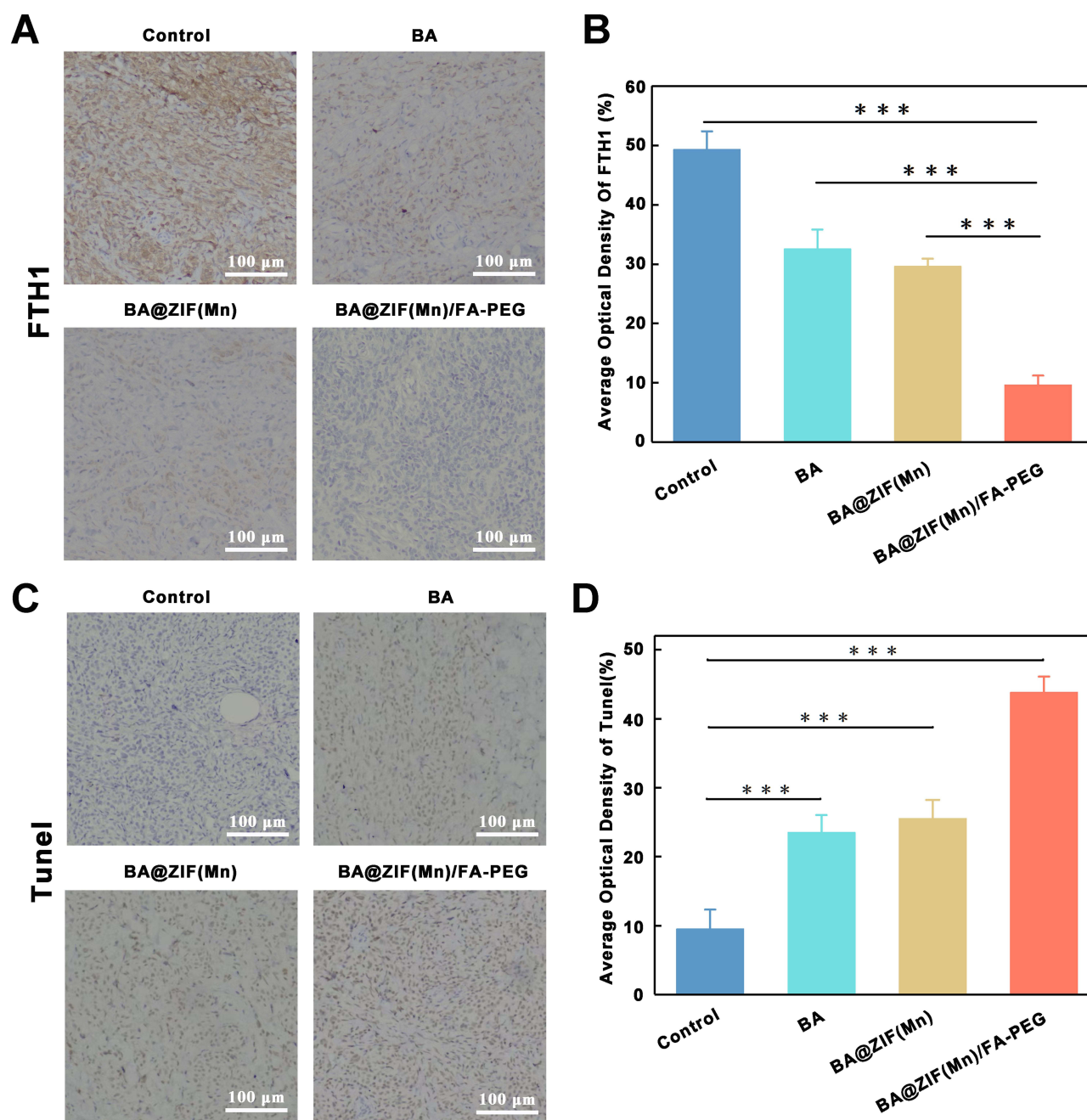


Figure 12 BA-Induced Ferroptosis in a Melanoma Xenograft Model. (A) Immunohistochemical FTH1 staining analysis of tumors from mice bearing B16-F10 melanoma treated with PBS, BA, BA@ZIF(Mn), and BA@ZIF(Mn)/FA-PEG. (B) Quantification of FTH1 immunohistochemical staining. (C) TUNEL staining analysis of tumors from mice treated with PBS, BA, BA@ZIF(Mn), and BA@ZIF(Mn)/FA-PEG. (D) Quantification of TUNEL staining. Scale bar = 100 μ m. Data are mean \pm SD (n = 3; ***p < 0.001).

Vivo Anti-Tumor Efficacy

To further validate the *in vivo* anti-tumor efficacy and biosafety of BA@ZIF(Mn)/FA-PEG NPs, we administered these NPs intravenously via the tail vein to mice bearing melanoma tumors. Analysis of tumor volume, tumor weight, body weight, and tumor growth inhibition (TGI) (Figures 11A–E) demonstrated that BA, BA@ZIF(Mn) NPs, and BA@ZIF(Mn)/FA-PEG NPs significantly suppressed tumor growth, with BA@ZIF(Mn)/FA-PEG NPs showing the most pronounced effect. Histological examination using H&E staining revealed substantial cell death in tumor tissues (Figure 11F). Notably, histological sections of the heart, liver, spleen, lungs, and kidneys showed no significant

abnormalities (Figure 11G), and there was no observable weight loss in the treated mice, indicating an absence of evident toxicity from BA@ZIF(Mn)/FA-PEG NPs following in vivo administration.

Further immunohistochemical and TUNEL staining analyses indicated that tumor cell death was primarily driven by apoptosis and ferroptosis. FTH1, a critical marker for ferroptosis, showed differential expression among treatment groups.^{8,56} Immunohistochemical staining (Figure 12A) revealed that FTH1 levels were highest in the control group, reflecting baseline ferroptosis-related activity. Quantification (Figure 12B) demonstrated a stepwise reduction in FTH1 expression, with BA@ZIF(Mn)/FA-PEG NPs showing the lowest FTH1 levels compared to other treatments, indicating a more efficient induction of ferroptosis through targeted delivery and controlled release.

TUNEL staining results (Figure 12C and D) corroborated these findings, demonstrating that apoptosis was induced by both BA and BA@ZIF(Mn) NPs, with BA@ZIF(Mn)/FA-PEG NPs inducing the highest levels of apoptosis among all groups. The dual induction of apoptosis and reduced ferroptosis activity indicates that BA@ZIF(Mn)/FA-PEG NPs effectively balance different cell death modalities, which may maximize therapeutic efficacy while minimizing potential off-target effects.

This dual cell death mechanism underscores the sophisticated anti-tumor capability of BA@ZIF(Mn)/FA-PEG NPs. By targeting both apoptosis and ferroptosis pathways, these nanoparticles provide a multifaceted therapeutic strategy that can overcome challenges related to limited drug accumulation in tumors, ultimately enhancing the efficacy of melanoma treatment.

Our results highlight the efficacy of BA@ZIF(Mn)/FA-PEG NPs in selectively inducing apoptosis and ferroptosis in tumor cells. The controlled modulation of BA concentrations within tumor tissues, facilitated by the targeted delivery mechanism, enables precise engagement of cell death pathways, thereby ensuring efficient tumor cell elimination. Additionally, the biosafety of BA@ZIF(Mn)/FA-PEG NPs was confirmed through histological analyses, which showed no toxicity in vital organs.

Conclusions

This study introduces manganese-doped ZIF-8 nanoparticles (BA@ZIF(Mn)/FA-PEG) encapsulating Baicalin as a novel platform for targeted melanoma therapy with integrated MR imaging. The nanoparticles demonstrate excellent biocompatibility and effectively address the challenge of limited drug accumulation in tumors, showing potent therapeutic efficacy.

While these results are promising, optimizing the delivery efficiency and stability of BA@ZIF(Mn)/FA-PEG nanoparticles in clinical settings remains a critical challenge. Future efforts should focus on refining drug release mechanisms and enhancing nanoparticle stability within the tumor microenvironment.

Additionally, our findings reveal the dual capacity of BA@ZIF(Mn)/FA-PEG nanoparticles to induce both ferroptosis and apoptosis, offering a multifaceted anti-tumor strategy. These characteristics position BA@ZIF(Mn)/FA-PEG as a promising candidate for advancing image-guided cancer therapies, with strong potential for clinical application in melanoma treatment.

Data Sharing Statement

All data are provided in the article and are available upon request from the corresponding author.

Author Contributions

All authors made a significant contribution to the work reported, whether that is in the conception, study design, execution, acquisition of data, analysis and interpretation, or in all these areas; took part in drafting, revising or critically reviewing the article; gave final approval of the version to be published; have agreed on the journal to which the article has been submitted; and agree to be accountable for all aspects of the work.

Funding

This study was financially supported by the Doctoral Startup Fund of the Affiliated Hospital of Shandong Second Medical University (No. 2021BKQ02), Shandong Second Medical University 2024 Affiliated Hospital Research and Development Fund (2024FYZ002) and the Funds for the Construction of Key Clinical Specialties of Traditional Chinese Medicine in Shandong Province.

Disclosure

The authors have declared that no competing interest exists.

References

- Geller AC, Clapp RW, Sober AJ, et al. Melanoma epidemic: an analysis of six decades of data from the Connecticut Tumor Registry. *J Clin Oncol*. 2013;31:4172–4178. doi:10.1200/JCO.2012.47.3728
- Ho H, Aruri J, Kapadia R, Mehr H, White MA, Ganesan AK. RhoJ regulates melanoma chemoresistance by suppressing pathways that sense DNA damage. *Cancer Res*. 2012;72:5516–5528. doi:10.1158/0008-5472.CAN-12-0775
- Trager MH, Queen D, Samie FH, Carvajal RD, Bickers DR, Geskin LJ. Advances in Prevention and Surveillance of Cutaneous Malignancies. *Am J Med*. 2020;133:417–423. doi:10.1016/j.amjmed.2019.10.008
- Ma W, Zhan R, Sui C, et al. Clinical Retrospective Analysis of 243 Patients with Rhinofacial Ulcers. *Clin Cosmet Invest Dermatol*. 2022;15:1475–1483. doi:10.2147/CCID.S371029
- Zhang D, Zhang W, Wu X, et al. Dual Modal Imaging-Guided Drug Delivery System for Combined Chemo-Photothermal Melanoma Therapy. *Int J Nanomed*. 2021;16:3457–3472. doi:10.2147/IJN.S306269
- Luke JJ, Flaherty KT, Ribas A, Long GV. Targeted agents and immunotherapies: optimizing outcomes in melanoma. *Nat Rev Clin Oncol*. 2017;14:463–482. doi:10.1038/nrclinonc.2017.43
- Yuan J, Khan SU, Yan J, Lu J, Yang C, Tong Q. Baicalin enhances the efficacy of 5-Fluorouracil in gastric cancer by promoting ROS-mediated ferroptosis. *Biomed Pharmacother*. 2023;164:114986. doi:10.1016/j.biopha.2023.114986
- Kong N, Chen X, Feng J, et al. Baicalin induces ferroptosis in bladder cancer cells by downregulating FTH1. *Acta Pharm Sin B*. 2021;11:4045–4054. doi:10.1016/j.apsb.2021.03.036
- Duan L, Zhang Y, Yang Y, et al. Baicalin Inhibits Ferroptosis in Intracerebral Hemorrhage. *Front Pharmacol*. 2021;12:629379. doi:10.3389/fphar.2021.629379
- Dou J, Wang Z, Ma L, et al. Baicalein and baicalin inhibit colon cancer using two distinct fashions of apoptosis and senescence. *Oncotarget*. 2018;9:20089–20102. doi:10.18632/oncotarget.24015
- Tsai PL, Tsai TH. Pharmacokinetics of baicalin in rats and its interactions with cyclosporin A, quinidine and SKF-525A: a microdialysis study. *Planta Med*. 2004;70:1069–1074. doi:10.1055/s-2004-832649
- Shen YC, Chiou WF, Chou YC, Chen CF. Mechanisms in mediating the anti-inflammatory effects of baicalin and baicalein in human leukocytes. *Eur J Pharmacol*. 2003;465:171–181. doi:10.1016/S0014-2999(03)01378-5
- Huang L, Peng B, Nayak Y, et al. Baicalein and Baicalin Promote Melanoma Apoptosis and Senescence via Metabolic Inhibition. *Front Cell Dev Biol*. 2020;8:836. doi:10.3389/fcell.2020.00836
- Zhang D, Zhang M, Pang Y, Li M, Ma W. Folic Acid-Modified Long-Circulating Liposomes Loaded with Sulfasalazine For Targeted Induction of Ferroptosis in Melanoma. *ACS Biomater Sci Eng*. 2024;10:588–598. doi:10.1021/acsbomaterials.3c01223
- Rodero CF, Luiz MT, Sato MR, et al. Rapamycin-loaded nanostructured lipid carrier modified with folic acid intended for breast cancer therapy. *Int J Pharm*. 2024;668:124954. doi:10.1016/j.ijpharm.2024.124954
- Nogueira E, Gomes AC, Preto A, Cavaco-Paulo A. Folate-targeted nanoparticles for rheumatoid arthritis therapy. *Nanomedicine*. 2016;12:1113–1126. doi:10.1016/j.nano.2015.12.365
- Oshiro-Junior JA, Sato MR, Boni FI, et al. Phthalocyanine-loaded nanostructured lipid carriers functionalized with folic acid for photodynamic therapy. *Mater Sci Eng C Mater Biol Appl*. 2020;108:110462. doi:10.1016/j.msec.2019.110462
- Kunuku S, Lin BR, Chen CH, et al. Nanodiamonds Doped with Manganese for Applications in Magnetic Resonance Imaging. *ACS Omega*. 2023;8:4398–4409. doi:10.1021/acsomega.2c08043
- Hao Y, Zheng C, Wang L, et al. Tumor acidity-activatable manganese phosphate nanoplatfor for amplification of photodynamic cancer therapy and magnetic resonance imaging. *Acta Biomater*. 2017;62:293–305. doi:10.1016/j.actbio.2017.08.028
- Ding B, Chen H, Tan J, et al. ZIF-8 Nanoparticles Evoke Pyroptosis for High-Efficiency Cancer Immunotherapy. *Angew Chem Int Ed Engl*. 2023;62:e202215307. doi:10.1002/anie.202215307
- Sun Y, Cao Z, Zhang X, et al. Rod-Shaped Au@Ce Nano-Platforms for Enhancing Photodynamic Tumor Collaborative Therapy. *Small Methods*. 2024. e2400945. doi:10.1002/smt.202400945
- Zhang X, Pant SM, Ritch CC, et al. Cell state dependent effects of Bmal1 on melanoma immunity and tumorigenicity. *Nat Commun*. 2024;15:633. doi:10.1038/s41467-024-44778-2
- Zhao L, Wang X, Lou H, et al. Buffet-style Cu(II) for enhance disulfiram-based cancer therapy. *J Colloid Interface Sci*. 2022;624:734–746. doi:10.1016/j.jcis.2022.06.009
- Wei Y, Pi C, Yang G, et al. LC-UV Determination of Baicalin in Rabbit Plasma and Tissues for Application in Pharmacokinetics and Tissue Distribution Studies of Baicalin after Intravenous Administration of Liposomal and Injectable Formulations. *Molecules*. 2016;21:444. doi:10.3390/molecules21040444
- Mi X, Hu M, Dong M, et al. Folic Acid Decorated Zeolitic Imidazolate Framework (ZIF-8) Loaded with Baicalin as a Nano-Drug Delivery System for Breast Cancer Therapy. *Int J Nanomed*. 2021;16:8337–8352. doi:10.2147/IJN.S340764
- Wang Y, Zhang M, Bi R, et al. ACSL4 deficiency confers protection against ferroptosis-mediated acute kidney injury. *Redox Biol*. 2022;51:102262. doi:10.1016/j.redox.2022.102262
- Deng Z, Chen M, Liu Y, et al. A positive feedback loop between mTORC1 and cathelicidin promotes skin inflammation in rosacea. *EMBO Mol Med*. 2021;13:e13560. doi:10.15252/emmm.202013560
- Ercolano G, De Cicco P, Rubino V, et al. Knockdown of PTGS2 by CRISPR/CAS9 System Designates a New Potential Gene Target for Melanoma Treatment. *Front Pharmacol*. 2019;10:1456. doi:10.3389/fphar.2019.01456
- Shi Z, Chen X, Zhang L, et al. FA-PEG decorated MOF nanoparticles as a targeted drug delivery system for controlled release of an autophagy inhibitor. *Biomater Sci*. 2018;6:2582–2590. doi:10.1039/C8BM00625C

30. Venna SR, Jasinski JB, Carreon MA. Structural evolution of zeolitic imidazolate framework-8. *J Am Chem Soc.* **2010**;132:18030–18033. doi:10.1021/ja109268m
31. Lahooti B, Akwii RG, Zahra FT, et al. Targeting endothelial permeability in the EPR effect. *J Control Release.* **2023**;361:4172–4178. doi:10.1016/j.jconrel.2023.07.039
32. Wang Y, Wang Z, Xu C, Tian H, Chen X. A disassembling strategy overcomes the EPR effect and renal clearance dilemma of the multifunctional theranostic nanoparticles for cancer therapy. *Biomaterials.* **2019**;197:284–293. doi:10.1016/j.biomaterials.2019.01.025
33. Kinoshita R, Ishima Y, Chuang VTG, et al. Improved anticancer effects of albumin-bound paclitaxel nanoparticle via augmentation of EPR effect and albumin-protein interactions using S-nitrosated human serum albumin dimer. *Biomaterials.* **2017**;140:162–169. doi:10.1016/j.biomaterials.2017.06.021
34. Liu S, Wang L, Zhang M, et al. Tumor Microenvironment-Responsive Nanoshuttles with Sodium Citrate Modification for Hierarchical Targeting and Improved Tumor Theranostics. *ACS Appl Mater Interfaces.* **2019**;11:25730–25739. doi:10.1021/acsami.9b07957
35. Chen Y, Minh LV, Liu J, et al. Baicalin loaded in folate-PEG modified liposomes for enhanced stability and tumor targeting. *Colloids Surf B Biointerfaces.* **2016**;140:74–82. doi:10.1016/j.colsurfb.2015.11.018
36. Fu J, Lu L, Li M, et al. A gamma-Glutamyl Transpeptidase (GGT)-Triggered Charge Reversal Drug-Delivery System for Cervical Cancer Treatment. *Vitro and in vivo Investigation Pharma.* **2023**;15.
37. Zheng H, Zhang Y, Liu L, et al. One-pot Synthesis of Metal-Organic Frameworks with Encapsulated Target Molecules and Their Applications for Controlled Drug Delivery. *J Am Chem Soc.* **2016**;138:962–968. doi:10.1021/jacs.5b11720
38. Amin K, Dannenfelser RM. In vitro hemolysis: guidance for the pharmaceutical scientist. *J Pharm Sci.* **2006**;95:1173–1176. doi:10.1002/jps.20627
39. Zahiri M, Kamali H, Abnous K, et al. Synthesis of folate targeted theranostic cubosomal platform for co-delivery of bismuth oxide and doxorubicin to melanoma in vitro and in vivo. *Eur J Pharm Biopharm.* **2024**;198:114259. doi:10.1016/j.ejpb.2024.114259
40. Maeda H. SMANCS and polymer-conjugated macromolecular drugs: advantages in cancer chemotherapy. *Adv Drug Deliv Rev.* **2001**;46:169–185. doi:10.1016/S0169-409X(00)00134-4
41. Horowitz LB, Shaham S. Apoptotic and Nonapoptotic Cell Death in Caenorhabditis elegans Development. *Annu Rev Genet.* **2024**;58:113–134. doi:10.1146/annurev-genet-111523-102051
42. Ai Y, Meng Y, Yan B, Zhou Q, Wang X. The biochemical pathways of apoptotic, necroptotic, pyroptotic, and ferroptotic cell death. *Mol Cell.* **2024**;84:170–179. doi:10.1016/j.molcel.2023.11.040
43. Carneiro BA, El-Deiry WS. Targeting apoptosis in cancer therapy. *Nat Rev Clin Oncol.* **2020**;17:395–417. doi:10.1038/s41571-020-0341-y
44. Yang B, Bai H, Sa Y, Zhu P, Liu P. Inhibiting EMT, stemness and cell cycle involved in baicalin-induced growth inhibition and apoptosis in colorectal cancer cells. *J Cancer.* **2020**;11:2303–2317. doi:10.7150/jca.37242
45. Wang Z, Ma L, Su M, et al. Baicalin induces cellular senescence in human colon cancer cells via upregulation of DEPP and the activation of Ras/Raf/MEK/ERK signaling. *Cell Death Dis.* **2018**;9:217. doi:10.1038/s41419-017-0223-0
46. Chen H, Gao Y, Wu J, et al. Exploring therapeutic potentials of baicalin and its aglycone baicalein for hematological malignancies. *Cancer Lett.* **2014**;354:5–11. doi:10.1016/j.canlet.2014.08.003
47. Wan D, Ouyang H. Baicalin induces apoptosis in human osteosarcoma cell through ROS-mediated mitochondrial pathway. *Nat Prod Res.* **2018**;32:1996–2000. doi:10.1080/14786419.2017.1359173
48. Green DR, Lillambi F. Cell Death Signaling. *Cold Spring Harb Perspect Biol.* **2015**;7:a006080. doi:10.1101/cshperspect.a006080
49. Shi Y. Caspase activation, inhibition, and reactivation: a mechanistic view. *Protein Sci.* **2004**;13:1979–1987. doi:10.1110/ps.04789804
50. Zhen Z, Xie J. Development of manganese-based nanoparticles as contrast probes for magnetic resonance imaging. *Theranostics.* **2012**;2:45–54. doi:10.7150/thno.3448
51. Ouyang S, Chen C, Lin P, et al. Hydrogen-Bonded Organic Frameworks Chelated Manganese for Precise Magnetic Resonance Imaging Diagnosis of Cancers. *Nano Lett.* **2023**;23:8628–8636. doi:10.1021/acs.nanolett.3c02466
52. Xie J, Liu G, Eden HS, Ai H, Chen X. Surface-engineered magnetic nanoparticle platforms for cancer imaging and therapy. *Acc Chem Res.* **2011**;44:883–892. doi:10.1021/ar200044b
53. Bogdanov A Jr, Mazzanti ML. Molecular magnetic resonance contrast agents for the detection of cancer: past and present. *Semin Oncol.* **2011**;38:42–54. doi:10.1053/j.seminoncol.2010.11.002
54. Hu X, Tang Y, Hu Y, et al. Gadolinium-Chelated Conjugated Polymer-Based Nanotheranostics for Photoacoustic/Magnetic Resonance/NIR-II Fluorescence Imaging-Guided Cancer Photothermal Therapy. *Theranostics.* **2019**;9:4168–4181. doi:10.7150/thno.34390
55. Clough TJ, Jiang L, Wong KL, Long NJ. Ligand design strategies to increase stability of gadolinium-based magnetic resonance imaging contrast agents. *Nat Commun.* **2019**;10:1420. doi:10.1038/s41467-019-09342-3
56. Tian Y, Lu J, Hao X, et al. FTH1 Inhibits Ferroptosis Through Ferritinophagy in the 6-OHDA Model of Parkinson's Disease. *Neurotherapeutics.* **2020**;17:1796–1812. doi:10.1007/s13311-020-00929-z